Future changes in extremes across China based on NEX-GDDP-CMIP6 models

Baogang Yang
Chongqing Climate center
Linxiao Wei (quiet7@126.com)
Chongqing Climate Center https://orcid.org/0000-0002-1241-6981
Hongyu Tang
Chongqing Climate Center
Yonghua Li
Chongqing Climate Center
Yong Wang
Chongqing Climate Center
Fen Zhang
Chongqing Climate Center
Jie Zhou
Chongqing Climate Center
Tianyu Zhang
Chongqing Climate Center
Tananbang Lv
People's Liberation Army Unit 31012

Research Article

Keywords: climate extremes, evaluation, projection, ensemble, NEX-GDDP-CMIP6

Posted Date: October 9th, 2023

DOI: https://doi.org/10.21203/rs.3.rs-3394039/v1

Abstract

In this study, we assess the performance of the NASA Earth Exchange Global Daily Downscaled Projections' (NEX-GDDP) CMIP6 models in simulating extreme climate indices over China and its eight subregions. Future projections of these indices for the period 2081–2100 are investigated under three scenarios. The findings suggest that the models reasonably reproduce the spatial patterns of absolute indices related to extreme temperature, except for the percentile indices. There are larger model spreads for warm days, heat wave frequency, and heat wave days. The models effectively capture the climatological distributions of most extreme precipitation indices, although limitations are observed for consecutive wet days (CWDs) and extremely heavy precipitation days (R50). Among the subregions, the multimodel ensemble performs best in simulating the spatial patterns of extreme climate indices in Northeast China. Compared to CMIP6 models, NEX-GDDP-CMIP6 exhibits enhanced capability in simulating the spatial distributions of extreme climate events, displaying higher spatial correlation coefficients and improved model consensus. Consistency among different models is high for temperature extremes, with northwest, southwest and southern regions projected to experience the most significant increase during the 21st century. Precipitation extremes are also projected to increase, except for consecutive dry days (CDDs). Inconsistencies among models are observed, particularly for the CDD and CWD indices in the whole country and for the total precipitation in the southern region. However, with higher emission scenarios, consistency improves for other precipitation indices. The extreme precipitation indices in Southwest, East and South China exhibit the most substantial and noticeable increases.

1. Introduction

In recent decades, the global temperature has been steadily rising. Between 2011 and 2020, the global average temperature increased by 1.09°C compared to the preindustrial period (1850–1900), primarily due to human activities (IPCC 2021). The IPCC AR6 Working Group I has pointed out that, irrespective of emission scenarios, the temperature rise is inevitably poised to exceed the 1.5°C threshold within 2020 to 2040. In fact, as of July 2023, global temperatures have surpassed the preindustrial levels by approximately 1.5°C, marking it as the highest global monthly average temperature in recorded human history (Climate Change Service 2023). Globally, human activities have resulted in an increased frequency and intensity of extreme weather events and climate incidents (Dong et al. 2020, 2022; Engdaw et al. 2023; Jiang et al. 2022; Lu et al. 2016; Madakumbura et al. 2021; Xu et al. 2022; Yin et al. 2017). This has escalated the risks of heatwaves, droughts, and floods, with profound implications for ecosystems, human health, and socioeconomic well-being (Fu and Wen 2002; Williams et al. 2015). As the warming trend continues to intensify, extreme climate events will pose critical threats to food and water security. Moreover, extreme events such as severe heatwaves, floods, droughts, and wildfires have become increasingly common in China. Beyond the threshold of temperature rise, the intensity and scope of these extreme climate events are bound to escalate further, with far-reaching consequences.

China's climate is significantly influenced by the East Asian monsoon and the Qinghai-Tibet Plateau, resulting in high climate sensitivity, large variability, and a wide range of extreme weather and climate events, often leading to frequent disasters (Chen et al. 2023; Cui et al. 2019; Duan and Wu 2005; Liu et al. 2023). In recent years, China has experienced multiple record-breaking extreme climate events. For instance, in the summer of 2023, a historically rare heavy precipitation event occurred in most parts of North China, with the maximum accumulated rainfall reaching 1003 mm in Licheng County, Xingtai, Hebei Province (National Climate Center of China 2023). In the summer of 2022, an extremely prolonged heatwave event affected the central and eastern regions of China, with the overall intensity of the heatwave being the strongest since 1961 (Ma and Yuan 2023). In 2021, Zhengzhou, Henan Province, experienced an unprecedented extreme rainfall event, with a maximum daily precipitation of 624 mm, close to the annual average precipitation of the station (641 mm), resulting in significant loss of life and extensive economic damage (Zhang et al. 2023). In the future, anthropogenic climate change will increase the occurrence of extreme weather and climate events in China, heightening the country's exposure to climate risks and leading to a lock-in effect (IPCC 2022). Therefore, it is essential to conduct high-precision estimations of the future evolution of extreme climate events in China and take proactive measures in advance.

Climate system models not only have the capability to simulate historical changes in global climate but also provide estimations of future variations, serving as crucial research tools for climate change detection and attribution. The previous CMIP5 models have demonstrated the ability to replicate the increasing spatial distribution of precipitation in China from northwest to southeast. However, they tend to underestimate precipitation in the coastal regions of southern China while overestimating precipitation in the northern part of the country and the Qinghai-Tibet Plateau (Chen et al. 2014). Additionally, they have shown good performance in simulating the climatic means and trends of precipitation extremes in China (Chen and Sun 2015). The simulations of precipitation extremes in the CMIP5 models have revealed wet deviations in western and northern China, accompanied by dry biases in southeastern China, as reported by Jiang et al. (2015). The sixth phase of the International Coupled Model Intercomparison Project (CMIP6) has witnessed the largest participation of models among all previous phases, providing critical data support for the IPCC-AR6 report. Compared to the climate models used in the previous phase, CMIP6 models feature higher resolutions, more intricate and refined physical processes, and utilize the latest shared socioeconomic pathways (SSPs) for future projections. Compared to the CMIP5 models, the CMIP6 models exhibit substantial improvements in simulating the dry bias in southern China and show compelling enhancements in capturing the climatological characteristics of extreme precipitation events (Chen et al. 2020; Xu et al. 2021; Zhu et al. 2021). CMIP6 models also perform better in simulating extreme temperature events in China than CMIP5 models (Yang et al. 2023). However, they still encounter difficulties in reproducing the spatial patterns of certain extreme temperature indices, such as TX90P (days with maximum temperature exceeding the 90th percentile) and heatwave events (Hirsch et al. 2021; Zhu et al. 2020). The differences in simulations between the two generations of models are mainly attributed to the upgraded physical schemes in the CMIP6 models (Zhu et al. 2020). Zhu et al. (2021) found that the spatial distributions of extreme indices in the 21st century projected by the CMIP5 and CMIP6 models are generally consistent. The projected results of the CMIP6 models indicate a significant increase in the TXX index (annual maximum of the daily maximum temperature) over northern China, while the southern region is expected to experience the most pronounced increases in TX90P and WSDI (warm spell duration index) (Zhang et al. 2021). In the future, apart from a decreasing trend in the CDD (consecutive dry days) index, various regions across China are expected to experience a significant increase in total precipitation, maximum consecutive 5-day precipitation, and the number of heavy rainfall days. Moreover, the CMIP6 simulations also indicate a greater increase in total precipitation and extreme precipitation over the Yangtze River basin and areas near 40°N (Zhu et al. 2021).

Although the CMIP6 models have shown significant improvements in simulating performance compared to previous model generations, there is still considerable uncertainty in the simulations and projections (Wei et al. 2023; Xu et al. 2021). This primarily stems from the models' inadequate representation of large-scale atmospheric circulation fields, deficiencies in physical parameterization schemes, challenges in accurately reproducing aerosol-radiation interactions and anthropogenic aerosol-cloud interactions' radiative forcing, and uncertainties in emission scenarios (Fan et al. 2022; Huang et al. 2013; Van Vuuren et al. 2011; Zhang et al. 2021; Zhou et al. 2014). In addition, the coarse resolution of the models poses challenges in capturing local-scale climate responses and hinders their application at the regional level. Therefore, it is imperative to apply correction and downscaling techniques to the model output before utilizing it. The National Aeronautics and Space Administration (NASA) has initiated a global daily data downscaling program, which has performed downscaling treatments on historical and projection experiments of 21 CMIP5 models. This program provides downscaled data at the global scale and high resolution while also correcting biases in both historical and projection experiments. These downscaled data exhibit excellent modeling capabilities for extreme climate events in China's region, offering more climate change information at the regional scale and reducing the uncertainty range of extreme precipitation events (Chen et al. 2017; Zhou et al. 2018). Recently, NASA released the latest version of these data (NEX-GDDP-CMIP6), which is based on the downscaling and correction of daily values using CMIP6 models (Thrasher et al. 2022). However, it remains unclear how the NEX-GDDP-CMIP6 model performs in simulating extreme climate events in China and in projecting the potential changes in these events.

This paper is organized as follows: Section 2 describes the observations, NEX-GDDP-CMIP6 data, methods and study area used in this study. Section 3 evaluates the results based on the simulations of the 26 NEX-GDDP-CMIP6 models and

multimodel ensemble (MME). The future changes in climate extremes projected by MME and climate model agreements are also explored in Section 3. The conclusion and discussion are given in Section 4.

2. Materials and methods

2.1. Datasets

The CN05.1 dataset is a comprehensive collection of daily observations that have been acquired since 1961 from more than 2,400 ground meteorological stations scattered across various regions within China. Employing the anomaly approach, distinct climate variables' climatic and anomaly fields were independently interpolated and subsequently integrated to generate gridded data (Wu and Gao 2013). The spatial resolution of this dataset is precisely defined as 0.25° × 0.25°. The daily maximum temperature and precipitation of this dataset were used to evaluate the climate models' simulation capabilities.

The model data utilized in this study incorporate daily maximum temperature and precipitation data under the historical experiment of 26 CMIP6 models from the Global Daily Downscaled Projections dataset by the National Aeronautics and Space Administration (NASA), as well as the model projections under the SSP1-2.6, SSP2-4.5, and SSP5-8.5 emission scenarios (Thrasher et al. 2022). The BCSD method, along with error correction and spatial downscaling, was applied to refine the CMIP6 historical and future projections. The dataset can be downloaded from the following website: https://www.nccs.nasa.gov/services/data-collections/land-based-products/nex-gddp-cmip6. The spatial resolution of the dataset is 0.25° × 0.25° (Table 1). In line with the PCC AR6 report, the reference period spanned from 1995 to 2014, while the projection period covered 2015 to 2100, with a specific focus on the long period of the 21st century (2081–2100).

Table 1
Information on the 26 climate models used in the study

	NEX-GDDP-CMIP6
Model	Total 26 models: ACCESS-CM2 ACCESS-ESM1-5 BCC-CSM2-MR CanESM5 CMCC-CM2-SR5 CMCC-ESM2 CNRM-CM6-1 CNRM-ESM2-1 EC-Earth3 EC-Earth3-Veg-LR GFDL-CM4 GFDL-ESM4 GISS-E2-1-G HadGEM3-GC31-LL INM-CM4-8 INM-CM5-0 IPSL-CM6A-LR KACE-1-0-G MIROC6 MIROC-ES2L MPI-ESM1-2-LR MRI-ESM2-0 NESM3 NorESM2-LM TaiESM1 UKESM1-0-LL
Simulation	Historical (1961–2014) SSP1-2.6 (2015–2100) SSP2-4.5 (2015–2100) SSP5-8.5 (2015–2100)
Variable	tasmax, pr
Temporal Resolution	Daily
Spatial Resolution	0.25°×0.25°

Under the SSP1-2.6 scenario, the CMCC-CM2-SR5 and GFDL-CM4 models do not have daily maximum temperature data, while the GFDL-CM4 model also lacks daily precipitation data.

2.2. Methods

We selected a total of 13 extreme climate indices as the primary focus, comprising 5 extreme temperature indices and 8 extreme precipitation indices (Table 2). To facilitate a concise summary of the results, the chosen indices were classified as follows: PTOT, SDII, RX1D, RX5D, and TXX were categorized as absolute indices; CDD and CWD were classified as duration indices; R20, R50, and T35 were designated as threshold-based indices; and TX90P, HWF, and HWD were denoted as percentile indices. Notably, TXX, TX90P, CDD, CWD, R20, R50, RX1D, RX5D, SDII, and PTOT were established and defined by the Expert Team on Climate Change Detection and Indices (ETCCDI), while T35, HWF, HWD, and R50 have also garnered widespread application in climate change research (Wu et al. 2023; Hirsch et al. 2021; Sun et al. 2011).

Table 2
Extreme temperature and precipitation indices

Indices	Definitions	Units
TXX	The annual maxima of daily maximum	℃
T35	Number of days with maximum temperature greater than and equal to 35 °C	day
TX90P	Percentage of days when Tmax larger than the 90th percentile	%
HWF	Annual count of heat waves (defined as 3 succeeding days with Tmax exceeding 90th percentile of the climatology)	time
HWD	Annual count of days for the heat waves	day
CDD	Maximum number of consecutive days with precipitation less than 1 mm	day
CWD	Maximum number of consecutive days with precipitation no less than 1 mm	day
R20	Annual count of days when precipitation greater than and equal to 20 mm	day
R50	Annual count of days when precipitation was greater than and/or equal to 50 mm	day
RX1d	Annual maximum 1-day precipitation	mm
RX5d	Annual consecutive maximum 5-day precipitation	mm
SDII	Annual total precipitation divided by the number of wet days in the year	mm/day
PTOT	Annual total precipitation in wet days	mm

For a comprehensive investigation of regional variations, we adopted the regional classification established by Zhou et al. (2014) to divide China into 8 subregions. These subregions included Northeast China (NEC; 39°–54°N, 119°–134°E), North China (NC; 36°–46°N, 111°–119°E), East China (EC; 27°–36°N, 116°–122°E), Central China (CC; 27°–36°N, 106°–116°E), Northwest China (NWC; 36°–46°N, 75°–111°E), the Tibetan Plateau (SWC1; 27°–36°N, 77°–106°E), Southwest China (SWC2; 22°–27°N, 98°–106°E), and South China (SC; 20°–27°N, 106°–120°E).

The Taylor diagram is a vital and concise tool used to assess the capabilities of models by examining the statistics concerning pattern correlation coefficients and the ratios of standard deviations (RSD) obtained from model outputs and observational data. A comprehensive elucidation of these statistics can be found in Taylor's work (2001). A close proximity of both the correlation coefficient and RSD to 1 signifies a strong performance by the model.

The Taylor skill score (TS) is a comprehensive index devised using pattern correlation coefficients and ratios of standard deviations (RSDs). The closer the TS score approaches 1, the stronger the simulation performance of the model. We calculated the Taylor skill scores (TS) for extreme climate indices simulated by individual models and the ensemble mean, as well as the TS scores for the eight subregions simulated by the multimodel ensemble (MME).

$$TS = \frac{4(1+R)^2}{\left(\frac{\sigma_{sm}}{\sigma_{to}} + \frac{\sigma_{to}}{\sigma_{sm}}\right)^2 (1+R_0)^2}$$

1

In this equation, R represents the pattern correlation coefficient, and R_0 equals 0.999, which is substituted into the formula as the maximum correlation coefficient among all models. σ_{sm} and σ_{so} denote the area-weighted ratios of standard deviations (RSDs) for the models and observations, respectively.

Simulated and projected changes in extreme climate indices in the long-term period (2081–2100) relative to the baseline period of 1995–2014 are calculated as follows:

When the indices' units are mm and mm/day:

Relative Change = $\frac{Index_{future} - Index_{baseline}}{Index_{baseline}} \times 100\%$ (2)

When the indices' units are %, ℃ and day:

Relative Change = $Index_{future} - Index_{baseline}$ (3)

3. Results

3.1. Performance of NEX-GDDP-CMIP6 models

First, an evaluation of the downscaling models' capability to simulate the climatology of extreme high-temperature events was conducted (Fig. 1). In the observations, the epicenter of extreme high temperatures resided in the northwestern region of China, with values surpassing 40℃. Other high-value areas were in North China and the Yangtze River Basin, where temperatures exceeded 37°C. The lowest values, below 15°C, could be found in the northwestern part of the Qinghai-Tibet Plateau. The NEX-GDDP-CMIP6 ensemble average closely aligned with observations, exhibiting a spatial correlation coefficient of 0.98. However, the model overestimated values in the northeastern region. The regions with high T35 index values were likewise situated in the northwestern part of China, as well as in North China and the Yangtze River Basin, where values exceeded 16 days. Low-value regions encompassed the southwest and northeastern parts of the country, with values below 0.5 days. The model ensemble average effectively simulated the number of hot days, with a spatial correlation coefficient reaching 0.88. Nevertheless, it overestimated and underestimated the number of hot days in the northeastern region and the area south of the Yangtze River, respectively. The high-value regions for TX90P were predominantly concentrated in western Yunnan Province, Guangdong Province, and other areas, with values exceeding 20%. Low-value regions were mainly observed in North China, with values below 12%. The model struggled to reproduce this distribution pattern, generally underestimating the percentage of warm days, with a spatial correlation coefficient of 0.51. However, the model ensemble average performed well in simulating the North China region. The high-value center of HWF was primarily found in Qinghai Province, western Tibet Autonomous Region, western Yunnan, Guangdong, and other places, with values exceeding 9 times. The low-value center appeared in North China, with values below 5 times. The model ensemble average underestimated most regions of the nation, particularly the western areas, exhibiting a spatial correlation coefficient of only 0.46. It performed relatively well in simulating the North China region. Regarding HWD, the high-value center predominantly occurred in the western region of China and Guangdong Province, where values exceeds 40 days. The low-value center was in North China and the northeastern region, with values below 24 days. The model ensemble average underestimated values in the eastern part of the NWC region, as well as the CC, EC, and SC regions, with a spatial correlation coefficient of 0.66, but it effectively simulated the remaining areas. In summary, the NEX-GDDP-CMIP6 ensemble average successfully simulated the spatial patterns of TXX and T35 and reasonably simulated the TX90P, HWF, and HWD indices in North China. However, it generally underestimated extreme high-temperature indices in other regions.

Further evaluation of the spatial patterns of extreme high-temperature events using Taylor diagram was conducted. Figure 2 illustrates the spatial correlation coefficients and standard deviation ratios between various model simulations, multimodel ensemble (MME) simulations, and observations for different extreme high-temperature indices. The results indicated that individual models and the ensemble average performed well in simulating the TXX index, with spatial correlation coefficients of approximately 0.98 and standard deviation ratios close to 1. The simulations for the T35 index were also relatively good, with spatial correlation coefficients exceeding 0.85. However, the standard deviation ratios were above 1.5. The models exhibited poor performance in simulating the TX90P index, with considerable discrepancies among different model results. The MME, BCC-CSM2-MR, INM-CM5-0, INM-CM4-8, and GISS-E2-1-G models demonstrated better performance, with spatial correlation coefficients of approximately 0.5, although their standard deviation ratios were less than 1. The latter three models outperformed the MME and BCC-CSM2-MR models. On the other hand, the ACCESS-ESM1-5, CMCC-CM2-SR5, MIROC6, and MIROC-ES2L models exhibited the poorest performance and exhibited a negative correlation with observations. The models also showed limited ability to simulate the HWF index, with scattered results on the Taylor diagram. The BCC-CSM2-MR model performed relatively well, with a spatial correlation coefficient exceeding 0.5 and a standard deviation ratio close to 1. On the other hand, the ACCESS-ESM1-5, CMCC-CM2-SR5, MIROC6, and MIROC-ES2L models continued to demonstrate a negative correlation with observations. The models' performance in simulating the HWD index was slightly better than that for TX90P and HWF. The MME, BCC-CSM2-MR, GISS-E2-1-G, and CNRM-CM6-1 models performed the best, with spatial correlation coefficients all exceeding 0.6. The ratio of their standard deviation to that of the observations was close to 1 for the GISS-E2-1-G and CNRM-CM6-1 models. Conversely, the ACCESS-ESM1-5, MIROC6, and MIROC-ES2L models exhibited poorer performance. The analysis indicated that the NEX-GDDP-CMIP6 model performed well in simulating TXX and T35, possibly due to the incorporation of observational data corrections. However, the corrected models had difficulties in simulating the TX90P, HWF, and HWD indices. These indices showed significant deviations from the observations, and there were considerable differences between the various models. Compared to the CMIP6 models, the NEX-GDDP-CMIP6 model improved its performance in representing TXX and TX90P. The downscaled dataset exhibited a higher spatial correlation with observations and significantly enhanced the consistency among models (Wei et al. 2023; Zhu et al. 2020).

The Taylor skill score provided a more intuitive evaluation of the climate model's ability to represent the climatology of the climate state. Figure 3 presents a histogram of the Taylor skill scores, where a score closer to 1 indicated a stronger model capability. In Fig. 3, both individual models and MME demonstrated strong model capabilities for the TXX index, with an MME Taylor skill score of 0.98, followed by the T35 index with a score of 0.67. However, the models exhibited weaker performance in capturing the climatology of the TX90P index over the China region, with an MME score of only 0.49. Nine models had a Taylor skill score exceeding 0.5, among which GISS-E2-1-G and INM-CM4-8 exhibited the highest capability for representing the TX90P climatology, with scores reaching 0.58. The models also showed limited skill in capturing the HWF index over the China region, with an MME score of 0.41. Five models had scores exceeding 0.5, and BCC-CSM2-MR demonstrated the highest capability for this index, reaching a score of 0.56. On the other hand, the HWD index obtained a higher score than TX90P and HWF, with an MME score of 0.6. Thirteen models had scores exceeding 0.5, with CNRM-CM6-1 performing the best and achieving a score of 0.68.

Table 3 presents the Taylor skill scores for different regions of China based on MME, along with the regional averages and anomalies. For the TXX index, MME exhibited the weakest spatial modeling capabilities for the EC region, with a Taylor skill score of only 0.63, while the NWC region demonstrated the strongest performance, with a score of 0.95. For the regional averages, the MME showed significant deviations in the NC and NEC regions, overestimating them by 2.69℃ and 2.73℃, respectively. Regarding the T35 index, the MME performed best in simulating the NWC region, achieving a score of 0.86. However, it exhibited limited modeling capabilities for the SWC2 and SWC1 regions, with scores close to 0. The MME showed the largest deviation in the EC region, exceeding 4.71 days. For the TX90P index, the MME demonstrated its strongest modeling capability for the NC region, with a Taylor skill score of 0.65, while it exhibited minimal performance for the NWC region, with a score of only 0.06. The largest deviation of the MME occurred in the NC region, with a value of -2.14%. For the HWF index, the MME's modeling capabilities were generally poor for most regions, except for the NEC region, where it obtained a score of 0.54. The region with the largest deviation from observations was SWC1, with a value of -1.31 times.

Regarding the HWD index, the MME demonstrated its weakest modeling capability for the CC region, with a Taylor skill score of 0.2, while performing best in simulating the NEC region, with a score of 0.69. The SC region showed the largest deviation in the simulations, underestimated by 6.26 days compared to observations. Overall, the MME performed best in simulating the NEC and NC regions, with most of the indices' scores exceeding 0.4. From a national perspective, the MME simulations tended to overestimate the TXX index and slightly overestimate the T35 index while underestimating the TX90P, HWF, and HWD indices, particularly in regions with complex terrain. Possible reasons for these discrepancies were the inaccuracies in the observational data used to calibrate CMIP6 model results and limitations inherent to the models themselves.

Table 3
Taylor skill scores for extreme high temperature indices in different regions of China and regional averages of observations and MME simulations. The value inside the parentheses represents the difference between historical experiments and observations.

		NWC	SWC2	SWC1	SC	CC	EC	NC	NEC	China
TXX	**TSS**	0.95	0.66	0.79	0.89	0.89	0.63	0.92	0.69	0.98
	OBS	32.02	30.28	20.10	35.28	35.35	36.30	33.35	32.33	30.12
	Historical	33.49	31.32	20.61	35.79	36.35	36.69	36.04	35.06	31.47
		(1.47)	(1.04)	(0.51)	(0.51)	(1.0)	(0.39)	(2.69)	(2.73)	(1.35)
T35	**TSS**	0.86	0	0.07	0.72	0.74	0.67	0.81	0.6	0.67
	OBS	10.81	0.04	0.44	6.67	8.82	12.29	2.84	0.71	5.45
	Historical	12.02	0.62	0.20	5.27	7.45	7.58	5.16	2.11	5.73
		(1.21)	(0.58)	(-0.24)	(-1.4)	(-1.37)	(-4.71)	(2.32)	(1.4)	(0.28)
TX90P	**TSS**	0.06	0.26	0.36	0.32	0.23	0.35	0.65	0.39	0.49
	OBS	16.98	17.93	17.65	15.78	15.04	14.81	15.72	14.65	16.34
	Historical	16.06	16.07	15.65	14.33	13.51	13.57	13.58	15.05	15.16
		(-0.92)	(-1.86)	(-2.0)	(-1.45)	(-1.53)	(-1.24)	(-2.14)	(0.4)	(-1.18)
HWF	**TSS**	0.1	0.17	0.35	0.2	0.17	0.22	0.48	0.54	0.41
	OBS	7.88	8.08	8.08	7.50	7.08	6.94	6.83	6.27	7.46
	Historical	7.02	7.40	6.77	6.67	6.19	5.97	5.73	6.34	6.63
		(-0.86)	(-0.68)	(-1.31)	(-0.83)	(-0.89)	(-0.97)	(-1.1)	(0.07)	(-0.83)
HWD	**TSS**	0.26	0.36	0.65	0.37	0.2	0.35	0.39	0.69	0.6
	OBS	36.25	29.27	26.90	39.85	31.14	29.36	39.83	32.38	34.21
	Historical	31.81	23.89	27.52	33.59	28.13	26.85	36.68	31.29	30.59
		(-4.44)	(-5.38)	(0.62)	(-6.26)	(-3.01)	(-2.51)	(-3.15)	(-1.09)	(-3.62)

Figure 4 presents the time series of four extreme high-temperature indices in China, averaged over the period 1961–2014, based on observations and simulations relative to 1995–2014. The time series TXX indicated that prior to the year 2000, the observed index consistently exceeded the MME values. However, after the year 2000, the observed and simulated changes showed a greater level of agreement. The trend coefficient differences between the observed and MME values were distinct, with values of -0.2°C per decade and 0.2°C per decade, respectively. Both coefficients passed the significance tests, emphasizing the difficulty of the MME in replicating the temporal characteristics of the TXX index. For the remaining four indices, the observational values exhibited an increasing trend over time, with trend coefficients of 0.3 days per decade, 1.8%

per decade, 0.9 events per decade, and 4.7 days per decade, respectively. The multimodel ensemble was generally successful in reproducing the trend changes for these indices, with trend coefficients of 0.5 days per decade, 1.6% per decade, 0.8 events per decade, and 4.3 days per decade, respectively. The observed and simulated extreme high temperature trends have passed the significance test at the 5% level. These results aligned closely with the original CMIP6 models, as bias correction methods failed to alter the trend changes in extreme events. Although the NEX-GDDP-CMIP6 models effectively captured the long-term trend characteristics of the latter four indices, they still exhibited limited capability in simulating interannual variations and amplitudes associated with these indices.

Figure 5 presents the spatial distribution of eight extreme precipitation indices, as observed and simulated by MME. The high-value center of the CDD index was in the northwestern region of China, ranging from 130 to 160 days. Conversely, low-value areas appeared in the southern parts of the country, ranging from 20 to 40 days. This pattern showed an increasing trend from the southeastern coastal areas toward the northwest inland. The MME could replicate this distribution pattern fairly well, with a spatial correlation coefficient of 0.82 compared to the observations. However, the MME noticeably overestimated the values in the northwestern region, with the center position being significantly larger and the values exceeding 160 days. This discrepancy may have been related to inaccuracies in the “observed” data used for model calibration. Regarding the CWD index, the high-value center was in the eastern part of the Qinghai-Tibet Plateau and the western part of the Sichuan Basin, with values exceeding 80 days. The low-value center appeared in the northwestern region of China, with values less than 3 days. This distribution pattern exhibited a north-to-south gradient. The MME could simulate this distribution pattern, with a spatial correlation coefficient of 0.6 compared to the observations. However, it struggled to reproduce the high-value center observed in the data, and it overestimated the values in the Yunnan region, as well as in the northeastern and northern parts of China. For the observed PTOT index, the high-value center was observed in the southeastern coastal areas, with values exceeding 1800 mm. The low-value center appeared in the northwestern region, with values less than 200 mm. This distribution pattern also demonstrated an increase from the southeast to the northwest. The MME was generally capable of reproducing the spatial distribution pattern observed in the data, with a spatial correlation coefficient of 0.95, which was the highest among all the extreme precipitation indices. However, compared to the original CMIP6 models, the MME still overestimated the precipitation over the southern part of the Qinghai-Tibet Plateau. The distribution pattern of the R20 index aligned with that of PTOT, with the high-value center still located in the southeastern coastal areas, exceeding 25 days. The MME could simulate the distribution pattern of R20 as well, with a spatial correlation coefficient of 0.81 compared to the observations. However, it overestimated the values on the southern side of the Qinghai-Tibet Plateau and underestimated the values in the southeastern coastal region, mostly concentrated around the Fujian, Jiangxi, and Anhui provinces. The distribution pattern of R50 was similar to that of R20, with the maximum value exceeding 5 days. The spatial correlation coefficient between the MME and the observations for the R50 index was 0.51, which was the lowest among all the extreme precipitation indices. This indicated a clear underestimation of the R50 index in the southern region of China. The observed distributions of RX1D, RX5D, and SDII were consistent with PTOT, increasing from northwest to southeast. The MME exhibited spatial correlation coefficients of 0.83, 0.89, and 0.86, respectively, compared to the observations. In the southeastern coastal region, the MME noticeably underestimated the values of these three indices, largely due to inaccuracies in the “observed data” used for calibration.

Figure 6 depicts the Taylor diagram for eight extreme precipitation indices. The NEX-GDDP-CMIP6 models performed the best in simulating the PTOT index, followed by the RX5D and SDII indices. The spatial correlation coefficients for all models were approximately 0.9, and the ratio of standard deviations was also close to 1. Regarding the CDD index, each model demonstrated good modeling capability with spatial correlation coefficients exceeding 0.8 and the ratio of standard deviations ranging from 1.0 to 1.5. However, the models exhibited weaker performance in simulating the CWD index, with spatial correlation coefficients of approximately 0.6 and a significant variation in the ratio of standard deviations, ranging from 0.5 to 1.6 among the different models. The simulation performance of the models for the R20 index was similar to that of the CDD index. The models exhibited the weakest capability in simulating the R50 index, with spatial correlation coefficients below 0.6 and ratios of standard deviations ranging from 0.5 to 1.5. The models performed relatively well in reproducing the spatial pattern of the RX1D index, with spatial correlation coefficients ranging from 0.8 to 0.9. However, the

ratio of standard deviations between the model results and observations was approximately 0.5, indicating an underestimation of the RX1D values. The NEX-GDDP-CMIP6 model showed a weaker capability in simulating the CWD and R50 indices but performed the best in simulating PTOT, RX5D, and SDII. Compared to the original CMIP6 model, the NEX-GDDP-CMIP6 showed better performance in capturing the spatial patterns of indices such as CDD, PTOT, and RX5D. Apart from the CWD index, the NEX-GDDP-CMIP6 model significantly reduced intermodel discrepancies and demonstrated good modeling capabilities for extreme precipitation events. (Wang et al. 2021; Wei et al. 2023; Xu et al. 2021; Zhu et al. 2020).

Figure 7 presents the Taylor skill scores for eight extreme precipitation indices. The models exhibited good performance in simulating the PTOT index, with values above 0.9. The RX5D and SDII indices ranked next, with most models achieving TS scores above 0.85. The modeling performance for the R20 and CDD indices was similar, with scores of approximately 0.75. Regarding the RX1D index, the models demonstrated TS scores of approximately 0.6, with the BCC-CSM2-MR, CMCC-CM2-SR5, CMCC-ESM2, GFDL-ESM4, and TaiESM1 models performing the best, achieving a TS score of 0.72. The MIROC-ES2L model performed the worst, with a TS score of 0.57. The modeling capability for the CWD index was comparable to that of the RX1D index, with TS scores of approximately 0.6. The CNRM-ESM2-1 model performed the best with a TS score of 0.68, while the CanESM5 model performed the worst with a TS score of 0.51. The scores for the R50 index were approximately 0.5, indicating the weakest modeling capability among the indices. The CMCC-CM2-SR5 model performed the best with a TS score of 0.62, while the CanESM5 model performed the worst with a score of 0.37. In summary, the MME exhibited strong modeling capability for the PTOT, RX5D, and SDII indices but performed the poorest in simulating the R50 index.

Table 4 provides the Taylor skill scores of extreme precipitation simulated by the MME for different regions in China, as well as the observed and simulated regional averages. For the CDD index, the MME exhibited the weakest modeling capability in the SWC1 region, with a score of only 0.52, while showing the best performance in simulating the EC region, with a score of 0.92. The MME overestimated most regions nationwide, with the largest deviation observed in the NWC region, where it exceeded the observed values by 38.79 days. Regarding the CWD index, the MME demonstrated limited modeling capability for the NWC and NC regions, with scores of only 0.1 and 0.19, respectively. The best simulation was observed in the EC region, with a score of 0.8. Overall, the MME tended to overestimate the CWD index, with the SWC2 region exhibiting the most significant overestimation, exceeding the observations by 16.59 days. For the PTOT index, the MME performed the worst in simulating the SWC1 region, with a TS score of 0.54, while achieving the highest score of 0.96 in the NC region. The MME simulation of the PTOT index generally fell short, particularly in the NWC region, where it was underestimated by 29.87%. Regarding the R20 index, the modeling capability of the MME was weakest in the SWC1 region, with a TS score of 0.13, while demonstrating the strongest capability in the NEC region, with a TS score of 0.86. The MME simulation of the R20 index had a tendency to underestimate, with the largest deviation observed in the SC region, falling short of observations by 11.68 days. The MME exhibited limited modeling capability for the R50 index in most regions, with the best performance observed in the NEC region, achieving a TS score of 0.7. The MME tended to underestimate the R50 index in various subregions, particularly in the SC region, where it fell short of observations by 3.23 days. For the RX1D index, the MME demonstrated the poorest modeling capability in the CC, EC, and SWC2 regions, with TS scores below 0.2, while achieving its best performance in the NEC region with a TS score of 0.81. The MME simulation of the RX1D index generally fell short of observations, with the SC region exhibiting the most significant underestimation, being 55.73% lower than the observed values. The MME performed relatively well in simulating the RX5D index, with the EC region showing weaker modeling capability, indicated by a TS score of only 0.24, while the NEC region exhibited the best simulation, with a TS score of 0.88. However, the MME still underestimated most regions, with the NWC region displaying the largest deviation, falling short of observations by 39.65%. The MME underestimated the SDII index in most regions. The largest deviation from observations occurs in the SC region, with an underestimation of 23.64%. The poorest simulated region was SWC1, with a TS score of 0.26, while the best simulated region was NEC, with a score of 0.83. Overall, the MME demonstrated varied modeling capabilities for different extreme precipitation indices and regions. It exhibited more consistent performance in the NEC region, with TS scores mostly exceeding 0.5 and smaller deviations from observations, possibly due to the GMFD dataset used to calibrate this set of data, which aligned closely with observations in the NEC region. The MME also performed reasonably well for the entire region of China, with TS scores surpassing 0.5.

Table 4

As in Table 3 but for eight precipitation indices (the differences between historical experiments and observations for PTOT, RX1D, RX5D and SDII are calculated as a percentile)

		NWC	SWC2	SWC1	SC	CC	EC	NC	NEC	China
CDD	TSS	0.67	0.84	0.52	0.58	0.75	0.92	0.55	0.69	0.74
	OBS	88.36	40.20	65.42	27.81	30.18	27.66	62.42	53.57	61.25
	Historical	127.15 (38.79)	35.25 (-4.95)	83.55 (18.13)	25.19 (-2.62)	34.59 (4.41)	28.73 (1.07)	84.93 (22.51)	78.39 (24.82)	82.5 (21.25)
CWD	TSS	0.1	0.44	0.4	0.55	0.63	0.8	0.19	0.5	0.64
	OBS	5.53	19.56	21.63	15.54	9.43	10.35	5.99	8.23	11.39
	Historical	4.22 (-1.31)	36.15 (16.59)	17.85 (-3.78)	24.53 (8.99)	15.73 (6.3)	16.69 (6.34)	9.33 (3.34)	10.55 (2.32)	12.8 (1.41)
PTOT	TSS	0.78	0.75	0.54	0.88	0.93	0.93	0.96	0.9	0.92
	OBS	179.63	1118.29	530.03	1616.55	1076.03	1313.08	433.13	535.23	596.72
	Historical	125.98 (-29.87)	1103.55 (-1.32)	534.79 (0.9)	1501.5 (-7.12)	987.63 (-8.22)	1215.3 (-7.45)	409.76 (-5.4)	512.38 (-4.27)	555.97 (-6.83)
R20	TSS	0.33	0.48	0.13	0.69	0.54	0.61	0.67	0.86	0.76
	OBS	0.41	11.54	1.46	21.97	13.64	17.89	3.82	3.78	5.27
	Historical	0.29 (-0.12)	2.36 (-9.18)	1.24 (-0.22)	10.29 (-11.68)	5.49 (-8.15)	10.7 (-7.19)	2.22 (-1.6)	2.14 (-1.64)	2.65 (-2.62)
R50	TSS	0.02	0	0.21	0.06	0	0.02	0.02	0.7	0.57
	OBS	0.02	0.55	0.12	3.45	1.86	2.91	0.39	0.27	0.66
	Historical	0 (-0.02)	0.02 (-0.53)	0.18 (0.06)	0.22 (-3.23)	0.04 (-1.82)	0.25 (-2.66)	0.03 (-0.36)	0.13 (-0.14)	0.33 (-0.33)
RX1D	TSS	0.55	0.19	0.4	0.44	0.16	0.18	0.29	0.81	0.67
	OBS	13.76	47.46	19.84	82.26	66.58	81.16	40.41	38.03	34.63
	Historical	13.4 (-2.62)	25.94 (-45.34)	19.29 (-2.77)	36.42 (-55.73)	31.94 (-52.03)	41.31 (-49.1)	27.57 (-31.77)	28.35 (-25.45)	23.06 (-33.41)
RX5D	TSS	0.74	0.63	0.39	0.66	0.37	0.24	0.76	0.88	0.89
	OBS	23.63	101.62	46.68	163.96	124.20	159.78	67.40	69.91	66.96
	Historical	14.26 (-39.65)	75.97 (-25.24)	49.87 (6.83)	103.91 (-36.62)	81.36 (-34.49)	101.59 (-36.42)	60.28 (-10.56)	63.11 (-9.73)	54.76 (-18.22)
SDII	TSS	0.58	0.57	0.26	0.8	0.59	0.48	0.61	0.83	0.85
	OBS	3.30	7.85	4.05	10.49	9.04	10.69	6.56	6.09	5.64
	Historical	3.71 (12.42)	6.32 (-19.49)	4.61 (13.83)	8.01 (-23.64)	6.93 (-23.34)	8.28 (-22.54)	5.96 (-9.15)	5.9 (-3.12)	5.29 (-6.21)

We assessed the temporal variability capability of the model regarding extreme precipitation indices in the Chinese region, and Fig. 8 presents the temporal evolution of eight extreme precipitation indices from 1961 to 2014 based on observations and model simulations. Except the CDD index, the observed values of the other extreme precipitation indices exhibited an increasing trend. The trend coefficients of observed CDD, CWD, R20, R50, RX1D, RX5D, SDII, and PTOT were − 1.46 days/10 years, 0.1 days/10 years, 0.03 days/10 years, 0.02 days/10 years, 0.87%/10 years, 0.34%/10 years, 0.34%/10 years, and 0.6%/10 years, respectively. The corresponding trend coefficients from the MME simulations were − 0.13 days/10 years, 0.01 days/10 years, 0.02 days/10 years, 0.01 days/10 years, 0.66%/10 years, 0.5%/10 years, 0.23%/10 years, and 0.12%/10 years, indicating overall agreement between the model simulations and observations. The trend coefficients of CDD, R50, and RX1D from observations and simulations passed a significance test at the 5% level, whereas CWD, R20, and PTOT did not pass the test. The trend coefficients of RX5D and SDII indices from MME simulations passed a significance test at the 5% level, whereas the observed values did not pass the test. However, except for the CWD index, the MME struggled to reproduce the interannual variability of the other extreme precipitation indices. This could be due to the small changes in the observed and simulated CWD, while the other indices exhibited significant variability. Regarding the CDD index, the MME values were obviously lower than the observed values before 1985, displaying a declining trend. After 1985, the trend stabilized, but the MME failed to capture this behavior. The observed CDD index demonstrated significant interannual and decadal variability, which the MME struggled to reproduce. The MME simulations approximated the values of the PTOT, R20, and R50 indices compared to observations but struggled to simulate their interannual variability. The observed RX1D, RX5D, and SDII indices exhibited quasiperiodic variations with significant interannual variability, which were also challenging for the MME to replicate accurately.

3.2. Future changes in extreme events

Given that multimodel ensembles (MMEs) generally outperform individual models in most cases, the projections of extreme temperature indices during 2081–2100 were obtained using the NEX-GDDP-CMIP6 MME under three scenarios: SSP1-2.6, ssp2-4.5, and SSP5-8.5. Figure 9 illustrates the spatial variability of the TXX, T35, TX90P, HWF, and HWD indices estimated by the MME. The dots represent regions where 90% of the models exhibited consistent signs with the multimodel ensemble average. Under the SSP1-2.6 scenario, the TXX index showed an increase nationwide (Fig. 9a), with a national average increase of 2.14℃ (Table 5). The increase in the northern region was greater than that in the southern region. However, there was considerable inconsistency among models in the SC and NEC regions. Under the SSP2-4.5 and SSP5-8.5 scenarios, the pattern of TXX index change remained consistent with the low-emission scenario, but the magnitude of increase became more significant. The TXX index increased by 3.2℃ and 5.57℃ nationwide under the SSP2-4.5 and SSP5-8.5 scenarios, respectively, and the consistency among models increased with higher emission scenarios. Similarly, the T35 index increased nationwide under the SSP1-2.6 scenario, with high-value centers appearing in the NWC and CC regions, exceeding 30 days, and a national average increase of 12.2 days. Under the SSP2-4.5 and SSP5-8.5 scenarios, the T35 index further increased, with national average increases of 19.26 days and 41.12 days, respectively. As emission scenarios increased, the range of high-value centers expanded. In the SSP5-8.5 scenario, except for the SWC1, SWC2, and NEC regions, most of the country experienced T35 index values exceeding 45 days, and the consistency among models remained high across all three emission scenarios. The TX90P index also increased with higher emission scenarios, exhibiting high consistency among models. Across the three scenarios, the national increases were 20.57%, 31.36%, and 51.18%, respectively. The NEC and NC regions showed relatively smaller increases compared to other regions. Regarding the HWF index, under the SSP1-2.6 scenario, the minimum value center appeared in the NEC region, with values below 6 occurrences nationwide (7.88 occurrences). Under the SSP2-4.5 scenario, the HWF increased nationwide, reaching 10.69 occurrences. In the SSP5-8.5 scenario, the HWF index values were smaller in the SWC1 and SWC2 regions compared to the previous two scenarios but increased in other regions with increasing emission scenarios, reaching 11.45 occurrences nationwide. The model consistency was lower in the SWC1 and SWC2 regions, while it remained high in other regions. The HWD index increased with higher emission scenarios, with the NEC region still exhibiting the minimum value center. The national values for the three scenarios were 70.13 days, 111.05 days, and 190.96 days, respectively. Overall, by the end of the 21st century, the

consistency among models regarding the change in extreme high-temperature events was high, with increases observed in most regions nationwide.

Table 5
Projected changes in the 13 extreme climate indices for 2081–2100 compared to 1995–2014 in the 8 subregions and China under the three scenarios

	Scenario	NWC	SWC2	SWC1	SC	CC	EC	NC	NEC	China
TXX	SSP1-2.6	2.29	2.02	2.19	1.73	2.23	2.16	2.37	2.22	2.14
(°C)	SSP2-4.5	3.45	2.90	3.26	2.55	3.29	2.96	3.45	3.28	3.20
	SSP5-8.5	6.01	5.01	5.46	4.65	5.51	5.13	5.59	5.68	5.57
T35	SSP1-2.6	13.47	7.24	3.89	16.72	17.77	18.35	11.07	5.00	12.20
(day)	SSP2-4.5	21.72	11.40	5.86	30.46	28.04	28.63	17.51	8.43	19.26
	SSP5-8.5	42.58	27.28	12.31	74.07	56.35	59.32	37.59	21.45	41.12
TX90P	SSP1-2.6	19.09	27.89	27.33	24.91	21.38	23.84	15.52	15.36	20.57
(%)	SSP2-4.5	29.87	40.97	42.11	37.18	30.68	33.82	23.67	23.31	31.36
	SSP5-8.5	49.43	59.73	64.91	56.39	48.81	52.88	40.52	42.49	51.18
HWF	SSP1-2.6	8.38	9.65	9.05	9.65	9.42	10.04	7.71	6.94	7.88
(time)	SSP2-4.5	12.21	11.06	12.12	11.88	12.48	12.90	11.50	9.71	10.69
	SSP5-8.5	13.82	8.37	9.36	10.73	14.43	14.03	16.05	13.36	11.45
HWD	SSP1-2.6	64.32	99.09	93.88	85.92	70.42	79.05	48.01	49.63	70.13
(day)	SSP2-4.5	105.22	150.22	150.88	133.73	105.75	117.41	77.33	78.28	111.05
	SSP5-8.5	185.25	226.29	245.93	211.89	178.04	194.74	143.75	154.01	190.96
CDD	SSP1-2.6	-1.68	-1.24	-1.74	0.23	-1.58	0.35	-2.00	-1.04	-1.41
(day)	SSP2-4.5	-2.59	0.35	-1.60	1.37	-0.92	1.11	-2.18	-1.61	-1.44
	SSP5-8.5	-3.11	0.87	-3.35	3.49	-0.90	2.00	-3.57	-2.86	-2.00
CWD	SSP1-2.6	0.28	3.19	1.94	2.14	0.95	1.16	1.00	1.46	1.35
(day)	SSP2-4.5	0.38	1.64	1.81	1.30	1.01	0.87	1.10	1.32	1.12
	SSP5-8.5	0.63	1.96	3.02	1.19	1.18	1.32	1.42	1.57	1.57
PTOT	SSP1-2.6	14.31	7.84	13.88	9.23	9.65	8.60	11.81	11.84	11.29
(%)	SSP2-4.5	20.66	5.75	18.29	7.26	8.89	8.53	13.34	11.99	13.63
	SSP5-8.5	33.24	10.62	34.68	8.86	14.46	11.80	23.48	17.05	21.99
R20	SSP1-2.6	0.13	1.46	1.07	2.66	1.65	2.19	0.63	0.78	1.14
(day)	SSP2-4.5	0.18	1.86	1.47	2.67	1.80	2.36	0.81	1.00	1.38
	SSP5-8.5	0.34	3.53	3.17	4.19	3.07	3.66	1.47	1.58	2.48
R50	SSP1-2.6	0.003	0.05	0.09	0.23	0.10	0.24	0.04	0.08	0.14
(day)	SSP2-4.5	0.004	0.06	0.16	0.27	0.13	0.31	0.06	0.11	0.20
	SSP5-8.5	0.01	0.14	0.37	0.52	0.25	0.53	0.10	0.21	0.41

	Scenario	NWC	SWC2	SWC1	SC	CC	EC	NC	NEC	China
RX1D	SSP1-2.6	11.31	15.31	12.79	14.92	14.46	12.24	11.58	13.56	11.88
(%)	SSP2-4.5	14.62	18.48	18.48	16.55	16.66	15.11	14.00	16.76	15.06
	SSP5-8.5	22.43	32.30	33.80	26.57	27.69	24.12	23.43	26.35	24.56
RX5D	SSP1-2.6	13.17	11.73	12.56	10.56	9.52	8.51	12.29	11.51	10.82
(%)	SSP2-4.5	16.94	14.71	18.40	11.40	10.67	10.70	13.83	13.35	13.67
	SSP5-8.5	26.99	25.88	34.13	20.25	19.10	16.81	24.11	20.75	22.45
SDII	SSP1-2.6	6.15	5.15	7.85	5.69	5.51	5.98	5.98	6.25	5.75
(%)	SSP2-4.5	7.90	6.10	10.93	6.27	6.64	7.05	7.26	7.42	7.42
	SSP5-8.5	12.93	10.93	20.47	10.15	11.29	11.01	13.11	11.48	12.59

Figure 10 depicts the temporal evolution of the national regional extreme high temperature indices estimated by MME under three emissions scenarios. The indices, namely, TXX, T35, TX90P, and HWD, all exhibited an increasing trend as time progressed. Moreover, as radiative forcing scenarios intensified, the magnitudes of these increases also escalated. By 2100, under the SSP1-2.6 scenario, the TXX, T35, TX90P, and HWD indices experienced respective augmentations of 1.83°C, 9.3 days, 18.62°C, and 62.07 days. Correspondingly, in the SSP2-4.5 scenario, these indices exhibited increases of 2.87℃, 16.32 days, 32.98%, and 115.53 days, respectively. In the SSP5-8.5 scenario, the same indices underwent more substantial amplifications of 6.37°C, 48.22 days, 59.37%, and 225.52 days. The HWF index demonstrated a growth trajectory with time under the low and medium emissions scenarios, albeit with a slower pace after 2060. However, a declining trend became noticeable beyond 2060 under the high emissions scenario, possibly attributable to an increase in the duration of individual heatwaves. Across these three scenarios, the HWF index experienced respective increments of 7.92 times, 11.9 times, and 11.43 times by the year 2100. From Fig. 10, it became apparent that most extreme high temperature indices continuously intensified with the amplification of emissions scenarios and the passage of time. Furthermore, higher emissions scenarios contributed to increased uncertainty among the models.

Figure 11 illustrates the spatial distribution characteristics of extreme precipitation events in the late 21st century under three emission scenarios. The CDD index was generally consistent among the three scenarios. It increased in southeastern China but decreased in other regions. In the southern part of the northwest region, the low-value center expanded with increasing emission scenarios. The distribution pattern of the CWD index was also similar under the three emission scenarios, showing an increasing trend nationwide. The high-value center around the southern side of the SWC1 region expanded with increasing emission scenarios. The simulation of these two indices by the model exhibited significant discrepancies, with scattered regions of only consistent signs in northern China. Under the low emission scenario, the PTOT index increased nationwide, with a high-value center appearing near the Kunlun Mountains, exceeding 20%. The regions of consistent sign deviation from the model climatology were in the SWC1, CC, and NEC regions. Under the moderate emission scenario, the high-value center near the Kunlun Mountains exceeded 30% and expanded further, with the region of consistent sign deviation moving northward. Under the high emission scenario, the range of the high-value center continued to expand, extending to the entire SWC1 region, and the region of consistent sign deviation in the NEC and NC regions also increased. In all three emission scenarios, the high-value center for the R20 index appeared in the SC region. With increasing emission scenarios, the values in this region continuously increased, and the range expanded. The highest value exceeded 5 days. Additionally, under the SSP5-8.5 scenario, a high-value center appeared south of the Qinghai-Tibet Plateau. Except for the NWC region, the region of consistent sign deviation increased in the other areas. The R50 index also increased with increasing emission scenarios, although the increase was relatively small. The high-value center appeared in the southeastern coastal region, while the change in other areas was minimal. The region of consistent sign deviation expanded with higher emission scenarios. The variations in the RX1D, RX5D, and SDII indices were relatively similar. These three

indices consistently increased nationwide under the low and moderate emission scenarios. Under the moderate emission scenario, high-value centers appeared near the Kunlun Mountains and on the eastern side of the NWC region. Under the high emission scenario, the values further increased, and the high-value center expanded to the entire SWC1 region, while the region of consistent sign deviation also expanded. Overall, except for the projected CDD index, which showed a distribution of fewer occurrences in the north and more in the south, the other precipitation indices consistently increased. The R20 and R50 indices showed significant increases in the southeastern coastal region, while the PTOT, RX1D, RX5D, and SDII indices primarily experienced significant increases in the western region. The CDD and CWD indices simulated by the MME exhibited significant inconsistencies among the models, whereas the PTOT index demonstrated high consistency in terms of sign only in the northern region of China, with substantial uncertainty persisting in the southern region. For the remaining indices, their consistency in terms of anomalies expanded continually as emission scenarios escalated.

Figure 12 illustrates the temporal variations in extreme precipitation indices estimated by the models. The CDD index exhibited a declining trend, with minimal differences in their long-term trends among the three emission scenarios. By 2100, the CDDs were projected to decrease nationwide by 0.8 days, 1.84 days, and 2.86 days under the three emission scenarios, respectively. Conversely, the CWD index showed a weak upward trend, with similarly small long-term trends across different emission scenarios. The CWD was projected to increase by 1.13 days, 1.21 days, and 2.34 days under the three emission scenarios, respectively. The R50 index also exhibited a minimal upward trend across the emission scenarios, although the long-term changes in the high emission scenario still surpassed those in the low and moderate emission scenarios. By 2100, the R50 index was projected to increase by 0.13 days, 0.22 days, and 0.58 days under the three scenarios, respectively. In the high emission scenario, starting from 2060, the values of the remaining extreme precipitation indices were significantly higher than those in the low and moderate emission scenarios. Under the high emission scenario, the PTOT, R20, RX1D, RX5D, and SDII indices increased by 24.93%, 3.21 days, 32.85%, 30.2 days, and 17.6%, respectively. The analysis above indicated that, except for the CDD and CWD indices, the other extreme precipitation indices exhibited clear increases under the high emission scenario, emphasizing the urgency of greenhouse gas mitigation.

The changes in the regional mean values of extreme indices over the period 2081–2100, compared to 1995–2014, are presented in Table 5. To illustrate, let us consider TXX in the extreme temperature index and PTOT in the extreme precipitation index.

Regarding the TXX index, the analysis revealed the following: In all three emission scenarios, the TXX index increased across all regions. In the low emission scenario, the most significant increase was observed in the NC region, with a value of 2.37℃. In the moderate emission scenario, the NWC and NC regions showed the most pronounced increase, with values of 3.45℃. In the high emission scenario, the NWC region exhibited the most significant increase, with a value of 6.01°C. The SC region experienced the smallest magnitude of increase among all regions. In the three emission scenarios, this region's values increased by 1.73℃, 2.55℃, and 4.65℃.

In addition, for the HWF index, the SWC2, SWC1, and SC regions showed a decrease in the change magnitude under the high emission scenario compared to the emission scenarios. However, the HWD index increased, suggesting an increase in the duration of individual heatwaves. In the high emission scenario, the NWC, SC, SWC1, NC, and SWC1 regions showed the most significant increases in the TXX, T35, TX90P, HWF, and HWD indices, respectively. These regions exhibited increases of 6.01 days, 74.07 days, 64.91%, 16.05 times, and 245.93 days, respectively. Overall, extreme heat events demonstrated an increasing trend in intensity as emission scenarios escalated.

Regarding the PTOT index, the analysis indicates the following: In general, these regions exhibited an increasing trend. However, under the moderate emission scenario, the values in the SWC2, SC, CC, and EC regions decreased compared to the low emission scenario. The NWC region showed the largest increase under the low and moderate emission scenarios, with values of 14.31% and 20.66%, respectively. In the high emission scenario, the greatest increase occurred in the SWC1 region. Under the low and moderate emission scenarios, the SWC2 region experienced the smallest increase, with increases of 7.84%

and 5.75%, respectively. In the high emission scenario, the SC region demonstrated the smallest increase, with an increase of 8.86%.

The changes in the CDD and CWD indices were inconsistent with other precipitation indices. The CDD index increased in the SWC2, SC, and EC regions as emission scenarios intensified, while the remaining regions exhibited the opposite pattern. The changes in the CWD index were more complex. The NWC and NC regions showed an increase in the CWD index as emission scenarios escalated. For the other regions, the CWD index initially decreased and then increased with increasing emission scenarios. Under the high emission scenario, the SC region exhibited the most significant increases in the CDD and R20 indices, while the SWC1 region experienced the most notable increases in the CWD, PTOT, RX1D, RX5D, and SDII indices, and the EC region showed the most significant increase in the R50 index. These indices increased by 3.49 days, 4.19 days, 3.02 days, 34.68%, 33.8%, 34.13%, 20.47%, and 0.53 days, respectively. In general, most extreme precipitation events in different regions of China increased with higher emission scenarios. These findings elucidated the potential implications of climate change in these specific regions. The intensification of such extreme climate indices under the SSP5-8.5 scenario underscored the urgency to mitigate greenhouse gas emissions and implement effective adaptation strategies to avert or minimize adverse impacts on local ecosystems, human societies, and vulnerability to climate risks.

4. Conclusion and discussion

We first evaluated the performances of the NEX-GDDP-CMIP6 models in simulating extreme climate indices over China and its 8 subregions and then investigated the future projections of these indices during 2081–2100 under the three scenarios. The results showed that the spatial patterns of absolute indices of extreme temperature events can be reasonably reproduced, while the percentile indices were difficult to simulate well. The models exhibited larger model spreads for TX90P, HWF and HWD. Except for TXX, the NEX-GDDP-CMIP6 MME could reasonably capture the trends of extreme temperature indices. The NEX-GDDP-CMIP6 models showed good abilities to capture the climatological distributions of extreme precipitation indices, except for the CWD and R50 indices. There are large intermodel uncertainties for simulating the two indices. The MME can simulate the trends of extreme precipitation indices, but it is difficult to simulate their interannual and decadal variabilities. MME exhibited diverse modeling capabilities across various regions and extreme indices. MME performs the best in simulating the spatial pattern of extreme climate indices in the NEC region among all subregions. In contrast to the CMIP6 models, NEX-GDDP-CMIP6 demonstrates an advanced capacity to simulate the spatial distributions of extreme climate events, showcasing superior spatial correlation coefficients and an enhanced level of model consensus.

The future changes in temperature and precipitation extremes under the three scenarios over China were further explored during the long period of the 21st century. Consistency among different models was found to be high for temperature extremes. Notably, the NWC, SC, SWC1, NC, and SWC1 subregions are projected to experience the most significant increase in extreme high temperature indices in the future. Specifically, for the entire country, the TXX, T35, TX90P, HWF, and HWD indices are projected to increase by 5.57 days, 41.12 days, 51.18%, 11.45 times, and 190.96 days, respectively, under the SSP5-8.5 scenario. In terms of precipitation extremes, there is a projected increase in indices such as CWD, PTOT, R20, R50, RX1D, RX5D, and SDII, while the CDD index is expected to decrease. On a national scale, during the long-term period of the 21st century, the CWD, PTOT, R20, R50, RX1D, RX5D, and SDII indices are projected to increase by 1.57 days, 21.99%, 2.48 days, 0.41 days, 24.56%, 22.45%, and 12.59%, respectively, while the CDD index is projected to decrease by 2 days. Considerable inconsistencies are observed among different models for the CDD and CWD indices in China. Additionally, great inconsistencies are also found for the PTOT index in southern China. With increasing emission scenarios, the consistency among models improves for other precipitation indices as well. Under the SSP5-8.5 scenario, the most pronounced increase is observed in the CDD and R20 indices in the SC region, the CWD, PTOT, RX1D, RX5D, and SDII indices in the SWC1 region, and the R50 index in the EC region. Importantly, limitations in the accuracy of the observational data used and deficiencies in the NEX-GDDP-CMIP6 models contribute to considerable uncertainty in estimating future extreme events in China. Therefore, continued efforts are necessary to address these limitations and improve the reliability of future projections. Moreover, in the forthcoming years, the probability of compound extreme events transpiring in China will surge,

demanding heightened research scrutiny and comprehensive investigation. Our findings indicate the necessity of implementing effective mitigation strategies to reduce greenhouse gas emissions and adapt to climate change.

Declarations

Conflict of interest

There are no conflicts of interest in this paper.

Funding

This work was jointly supported by the National Natural Science Foundation of China (Grants Nos. 41875111), China Meteorological Administration Innovation and Development Project (Grant No. CXFZ2021Z011 and CXFZ2021Z005) and Chongqing Natural Science Foundation Project (Grant No.CSTB2022NSCQ-MSX0558 and cstc2021jcyj-msxmX0913)

Data availability

The CN05.1 data is available at https://ccrc.iap.ac.cn/resource/detail?id=228. The NEX-GDDP-CMIP6 data is available at https://www.nccs.nasa.gov/services/data-collections/land-based-products/nex-gddp-cmip6.

Code availability

NCL and CDO softwares were used for coding the methods as described in the methodology section.

Author contributions

Yang Baogang prepared the figures and wrote the main manuscript. Wei linxiao performed analysis on the extreme indices. Tang Hongyu participated in the analysis and revision of the manuscript. Li Yonghua, Wang Yong, Zhang Fen, Zhou Jie, Zhang Tianyu and Lv Tananbang contributed to download the model data, refine the discussions, read and approved the final manuscript.

References

1. Chen H, Sun J (2015) Assessing model performance of climate extremes in China: an intercomparison between CMIP5 and CMIP3. Clim Change 129:197-211. https://doi.org/10.1007/s10584-014-1319-5
2. Chen H, Sun J, Lin W, Xu H (2020) Comparison of CMIP6 and CMIP5 models in simulating climate extremes. Sci Bull 65:1415-1418. https://doi.org/10.1016/j.scib.2020.05.015
3. Chen HP, Sun JQ, Li HX (2017) Future changes in precipitation extremes over China using the NEX-GDDP high-resolution daily downscaled data-set. Atmos Ocean Sci Lett 10:403-410. https://doi.org/10.1080/16742834.2017.1367625
4. Chen L, Chen W, Hu P, Chen S, An X (2023) Climatological characteristics of the East Asian summer monsoon retreat based on observational analysis. Clim Dyn 60:3023-3037. https://doi.org/10.1007/s00382-022-06489-6
5. Chen X, Xu Y, Xu C, Yao Y (2014) Assessment of precipitation simulations in China by CMIP5 multi-models. Adv Clim Change Res 10:217
6. Climate Change Service (2023) European union's copernicus climate change service. Copernicus Services website https://climate.copernicus.eu/surface-air-temperature-july-2023
7. Cui D, Wang C, Santisirisomboon J (2019) Characteristics of extreme precipitation over eastern Asia and its possible connections with Asian summer monsoon activity. Int J Climatol 39:711-723. https://doi.org/10.1002/joc.5837
8. Dong S, Sun Y, Li C (2020) Detection of human influence on precipitation extremes in Asia. J Clim 33:5293-5304. https://doi.org/10.1175/JCLI-D-19-0371.1

9. Dong T, Zhu X, Deng R, Ma Y, Dong W (2022) Detection and attribution of extreme precipitation events over the Asian monsoon region. Weather Clim Extrem 38:100497. https://doi.org/10.1016/j.wace.2022.100497
10. Duan AM, Wu GX (2005) Role of the tibetan plateau thermal forcing in the summer climate patterns over subtropical Asia. Clim Dyn 24:793-807. https://doi.org/10.1007/s00382-004-0488-8
11. Engdaw MM, Steiner AK, Hegerl GC, Ballinger AP (2023) Attribution of observed changes in extreme temperatures to anthropogenic forcing using CMIP6 models. Weather Clim Extrem 39:100548. https://doi.org/10.1016/j.wace.2023.100548
12. Fan T, Liu X, Wu C, Zhang Q, Zhao C, Yang X, Li Y (2022) Comparison of the anthropogenic emission inventory for CMIP6 models with a country-level inventory over China and the simulations of the aerosol properties. Adv Atmos Sci 39:80-96. https://doi.org/10.1007/s00376-021-1119-6
13. Fu C, Wen G (2002) Several issues on aridification in the Northern China. Clim Environ Res 7:22-29
14. Hirsch AL, Ridder NN, Perkins-Kirkpatrick SE, Ukkola A (2021) CMIP6 multimodel evaluation of present-day heatwave attributes. Geophys Res Lett 48:e2021GL095161. https://doi.org/10.1029/2021GL095161
15. Huang DQ, Zhu J, Zhang YC, Huang AN (2013) Uncertainties on the simulated summer precipitation over Eastern China from the CMIP5 models. J Geophys Res Atmos 118:9035-9047. https://doi.org/10.1002/jgrd.50695
16. IPCC (2021) Summary for policymakers In: Masson-Delmotte V, Zhai P, Pirani S, Connors C, Péan S, Berger N, Caud Y, Chen L, Goldfarb M, Monteiro PMS (eds) Climate change 2021: the physical science basis Contribution of working group I to the sixth assessment report of the intergovernmental panel on climate change. Cambridge University Press, Cambridge, UK
17. IPCC (2022) climate change 2022: impacts, adaptation, and vulnerability. Cambridge University Press, Cambridge, UK
18. Jiang W, Chen H, Shi Z (2022) Anthropogenic influence on extreme temperature changes over the mid–high latitudes of Asia. Int J Climatol 42:8619-8631. https://doi.org/10.1002/joc.7753
19. Jiang Z, Li W, Xu J, Li L (2015) Extreme precipitation indices over china in CMIP5 Models. Part I: model evaluation. J Clim 28:8603-8619. https://doi.org/10.1175/JCLI-D-15-0099.1
20. Liu Z, Lee SS, Nellikkattil AB, Lee JY, Dai L, Ha KJ, Franzke CLE (2023) The East Asian summer monsoon response to global warming in a high resolution coupled model: mean and extremes. Asia-Pac J Atmos Sci 59:29-45. https://doi.org/10.1007/s13143-022-00285-2
21. Lu C, Sun Y, Wan H, Zhang X, Yin H (2016) Anthropogenic influence on the frequency of extreme temperatures in China. Geophys Res Lett 43:6511-6518. https://doi.org/10.1002/2016GL069296
22. Ma F, Yuan X (2023) When will the unprecedented 2022 summer heat waves in yangtze river basin become normal in a warming climate? Geophys Res Lett 50:e2022GL101946. https://doi.org/10.1029/2022GL101946
23. Madakumbura GD, Thackeray CW, Norris J, Goldenson N, Hall A (2021) Anthropogenic influence on extreme precipitation over global land areas seen in multiple observational datasets. Nat Commun 12:3944. https://doi.org/10.1038/s41467-021-24262-x
24. Sun J, Wang H, Yuan W (2011) Decadal Variability of the Extreme Hot Event in China and Its Association with Atmospheric Circulations. CLIM RES 16: 199-208. https://doi.org/10.3878/j.issn.1006-9585.2011.02.09
25. Thrasher B, Wang W, Michaelis A, Melton F, Lee T, Nemani R (2022) NASA global daily downscaled projections, CMIP6. Sci Data 9:262. https://doi.org/10.1038/s41597-022-01393-4
26. Van Vuuren DP, Edmonds J, Kainuma M et al (2011) The representative concentration pathways: an overview. Clim Change 109:5. https://doi.org/10.1007/s10584-011-0148-z
27. Wang Y, Li H, Wang H, Sun B, Chen H (2021) Evaluation of CMIP6 model simulations of extreme precipitation in China and comparison with CMIP5. Acta Meteorol Sin 79:369-386
28. Wei L, Xin X, Li Q, Wu Y, Tang H, Li Y, Yang B (2023) Simulation and projection of climate extremes in China by multiple coupled model intercomparison project phase 6 models. Int J Climatol 43:219-239. https://doi.org/10.1002/joc.7751

29. Williams AP, Seager R, Abatzoglou JT, Cook BI, Smerdon JE, Cook ER (2015) Contribution of anthropogenic warming to California drought during 2012–2014. Geophys Res Lett 42:6819-6828. https://doi.org/10.1002/2015GL064924
30. Wu J, Gao XJ (2013) A gridded daily observation dataset over China region and comparison with the other datasets (in Chinese). Chin J Geophys 56:1102-1111. https://doi.org/10.6038/cjg20130406
31. Wu X, Wang L, Niu Z, Jiang W, Cao Q (2023) More extreme precipitation over the Yangtze River Basin, China: Insights from historical and projected perspectives. Atmos Res: 106883. https://doi.org/10.1016/j.atmosres.2023.106883.
32. Xu H, Chen H, Wang H (2021) Future changes in precipitation extremes across China based on CMIP6 models. Int J Climatol 42:635-651. https://doi.org/10.1002/joc.7264
33. Xu H, Chen H, Wang H (2022) Detectable human influence on changes in precipitation extremes across China. Earth's Future 10:e2021EF002409. https://doi.org/10.1029/2021EF002409
34. Yang Y, Zhang Y, Gao Z, Pan Z, Zhang X (2023) Historical and projected changes in temperature extremes over China and the inconsistency between multimodel ensembles and individual models from CMIP5 and CMIP6. Earth Space Sci 10:e2022EA002514. https://doi.org/10.1029/2022EA002514
35. Yin H, Sun Y, Wan H, Zhang X, Lu C (2017) Detection of anthropogenic influence on the intensity of extreme temperatures in China. Int J Climatol 37:1229-1237. https://doi.org/10.1002/joc.4771
36. Zhang G, Zeng G, Yang X, Jiang Z (2021) Future changes in extreme high temperature over China at 1.5°C–5°C global warming based on CMIP6 simulations. Adv Atmos Sci 38:253-267. https://doi.org/10.1007/s00376-020-0182-8
37. Zhang Q, Li R, Sun J, Lu F, Xu J, Zhang F (2023) A review of research on the record-breaking precipitation event in henan province, China, July 2021. Adv Atmos Sci 40:1485-1500. https://doi.org/10.1007/s00376-023-2360-y
38. Zhou B, Wen QH, Xu Y, Song L, Zhang X (2014) Projected changes in temperature and precipitation extremes in China by the CMIP5 multimodel ensembles. J Clim 27:6591-6611. https://doi.org/10.1175/JCLI-D-13-00761.1
39. Zhou L, Lan M, Cai R, Wen P, Yao R, Yang Y (2018) Projection and uncertainties of extreme precipitation over the Yangtze River valley in the early 21st century. Acta Meteor Sin 76:47-61
40. Zhu H, Jiang Z, Li J, Li W, Sun C, Li L (2020) Does CMIP6 inspire more confidence in simulating climate extremes over China? Adv Atmos Sci 37:1119-1132. https://doi.org/10.1007/s00376-020-9289-1
41. Zhu H, Jiang Z, Li L (2021) Projection of climate extremes in China, an incremental exercise from CMIP5 to CMIP6. Sci Bull 66:2528-2537. https://doi.org/10.1016/j.scib.2021.07.026

Figures

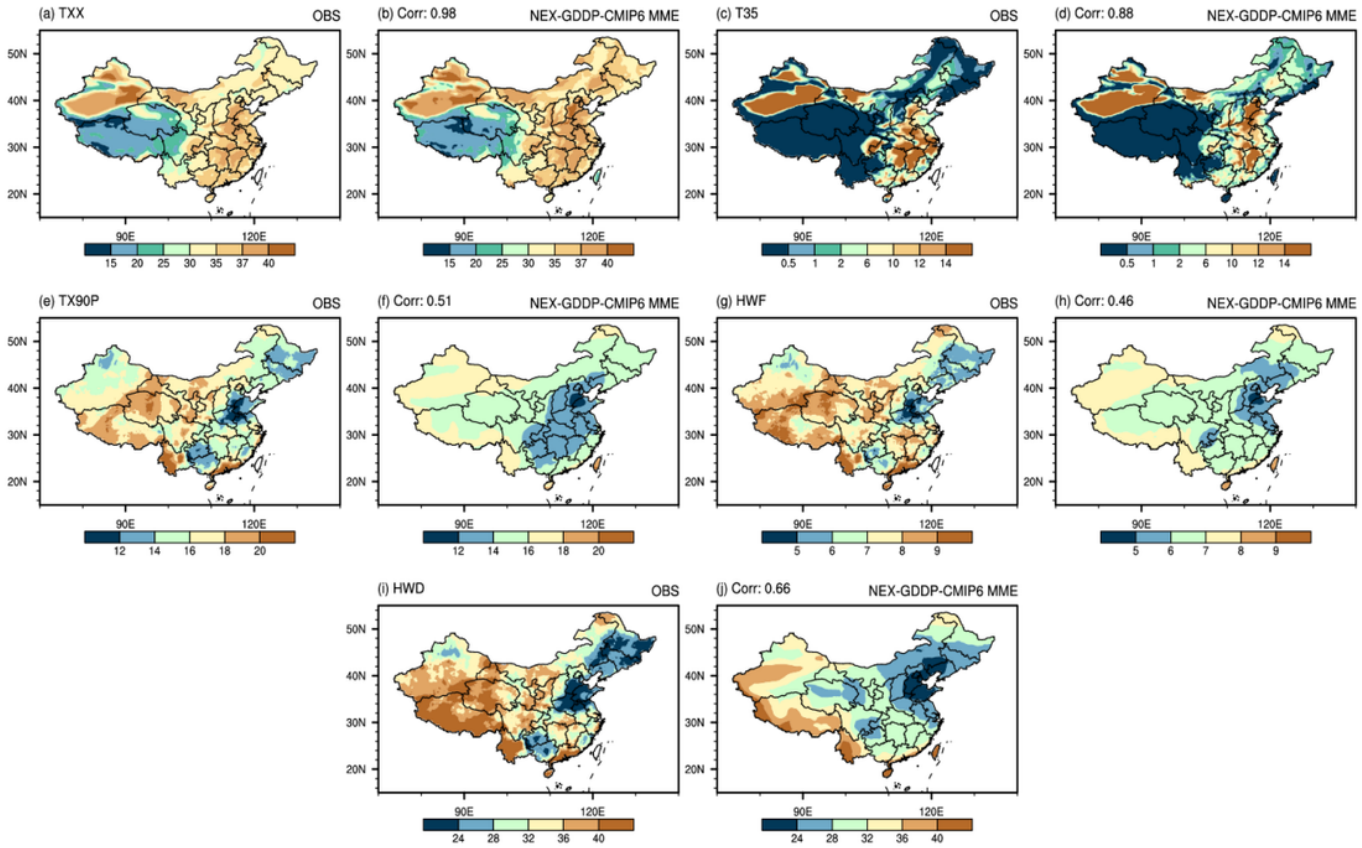

Figure 1

Spatial distributions of TXX (a, b), T35 (c, d), TX90P (e, f), HWF (g, h) and HWD (i, j) from the observation (a, c, e, g, i) and multimodel ensemble (MME) mean of 26 NEX-GDDP-CMIP6 models (b, d, f, h, j) over China during 1995-2014

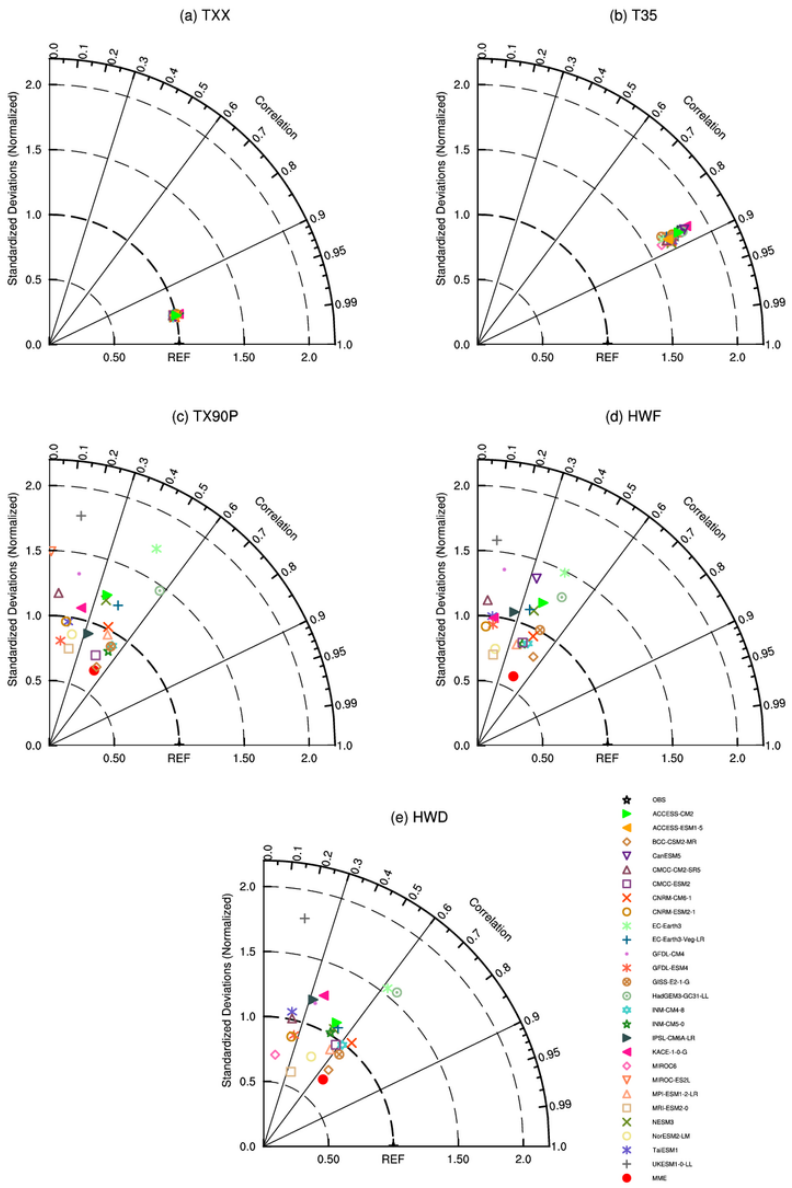

Figure 2

Taylor diagrams of the NEX-GDDP-CMIP6-simulated climatic means (1995-2014) for five extreme temperature indices over China. The azimuthal position represents the pattern spatial correlation, and the radial distance from the origin represents the spatial variability

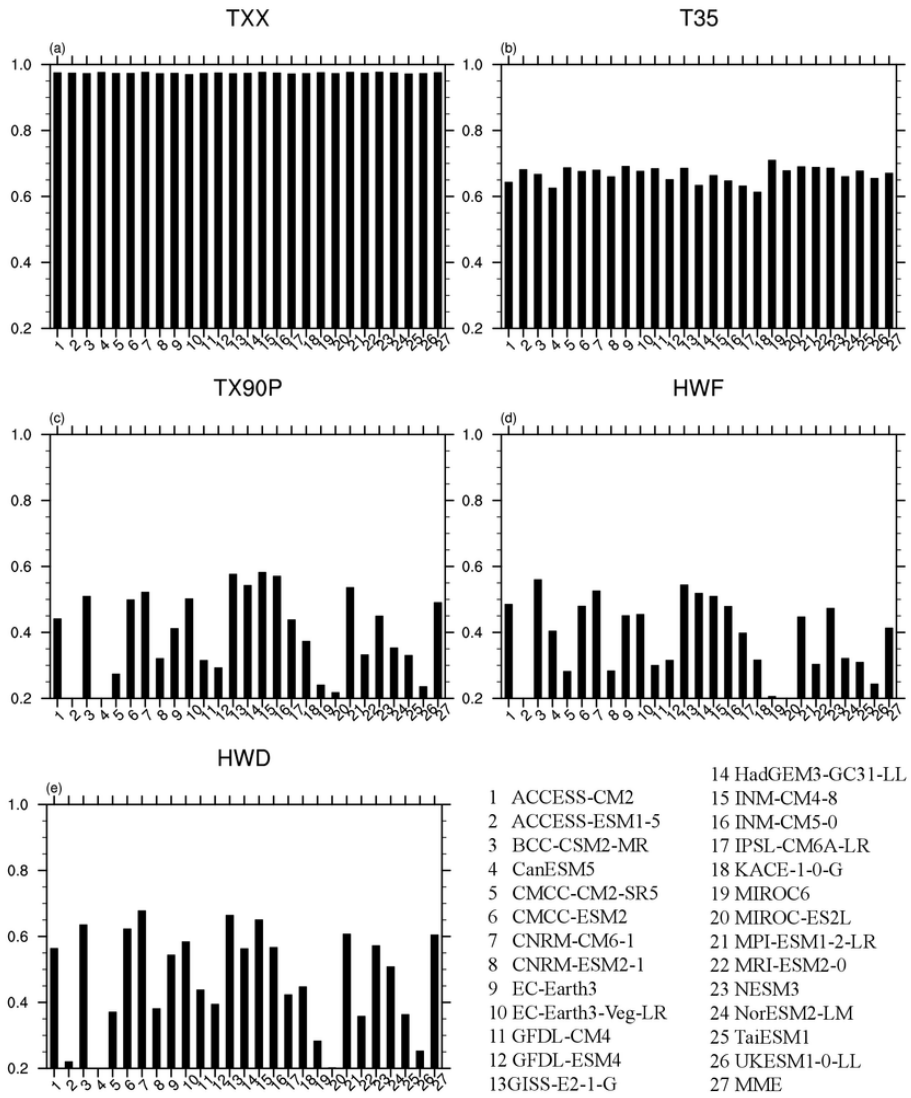

Figure 3

Taylor skill scores of 26 CMIP6 models and their ensemble mean in simulating extreme temperature over China

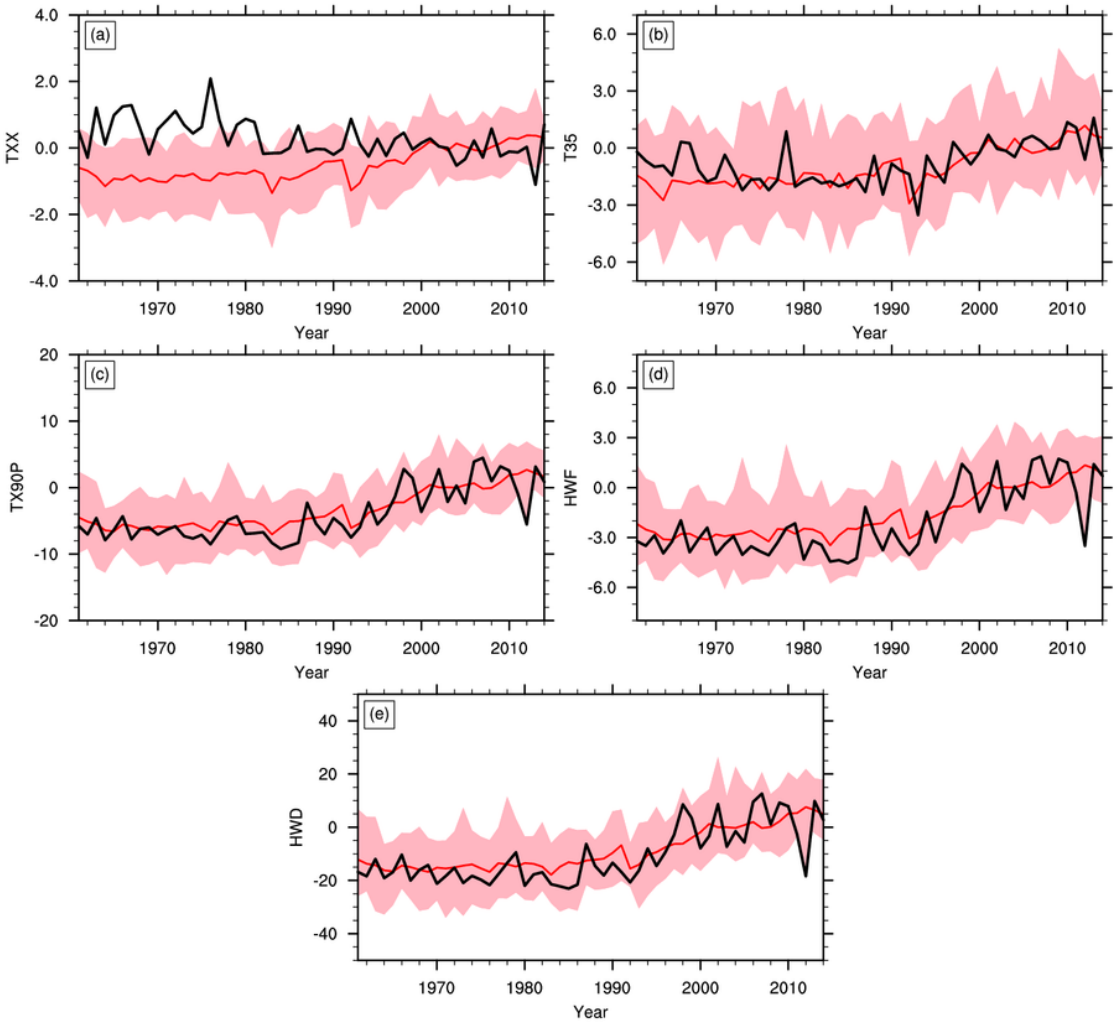

Figure 4

Time series of five extreme temperature indices over China during 1961–2100 relative to the period 1995–2014. The black and red lines indicate the corresponding results from the observations and MME of 26 model simulations. The top and bottom bounds of the shaded area are the maximum and minimum values of 26 CMIP6 model simulations.

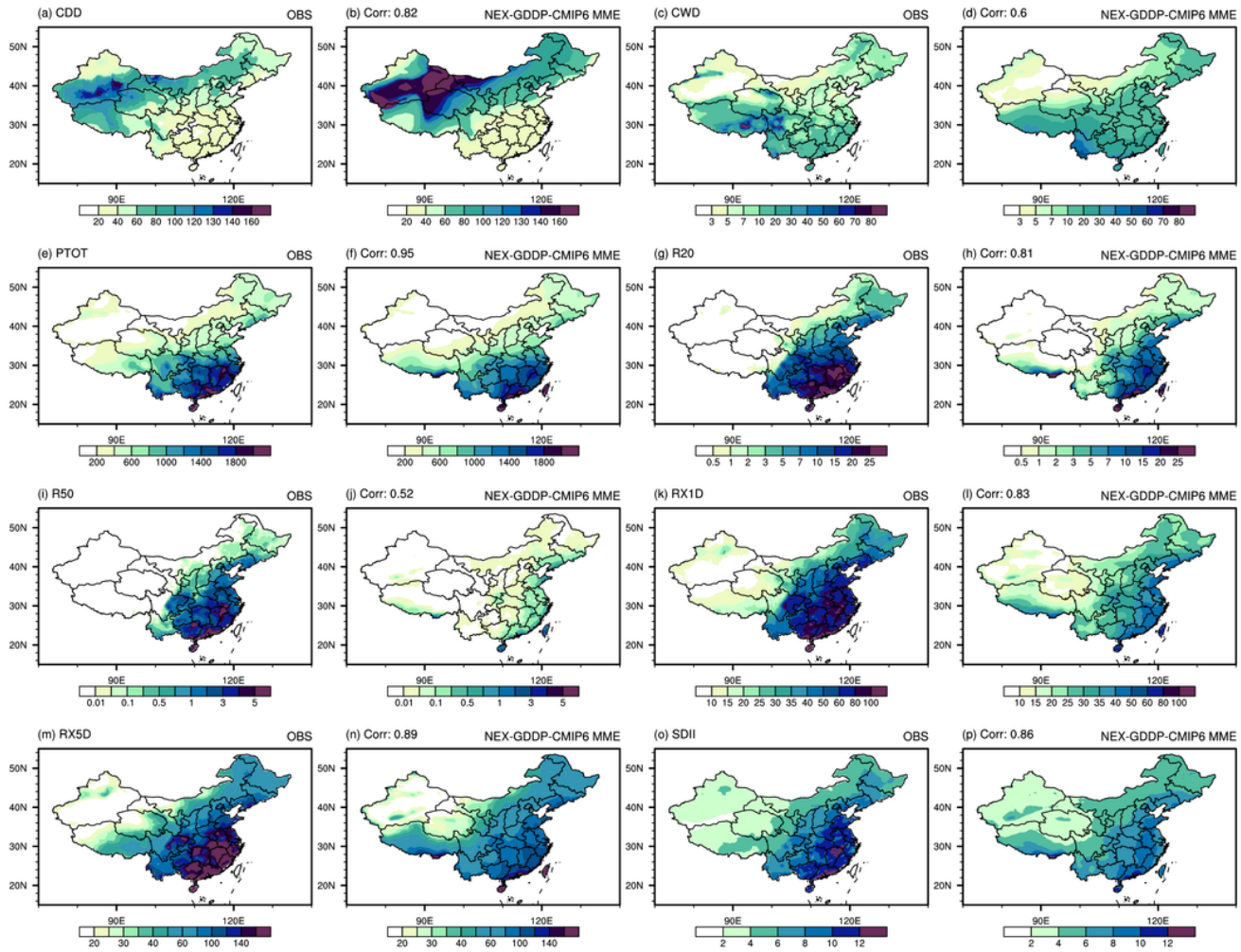

Figure 5

As in Fig. 1 but for eight precipitation indices

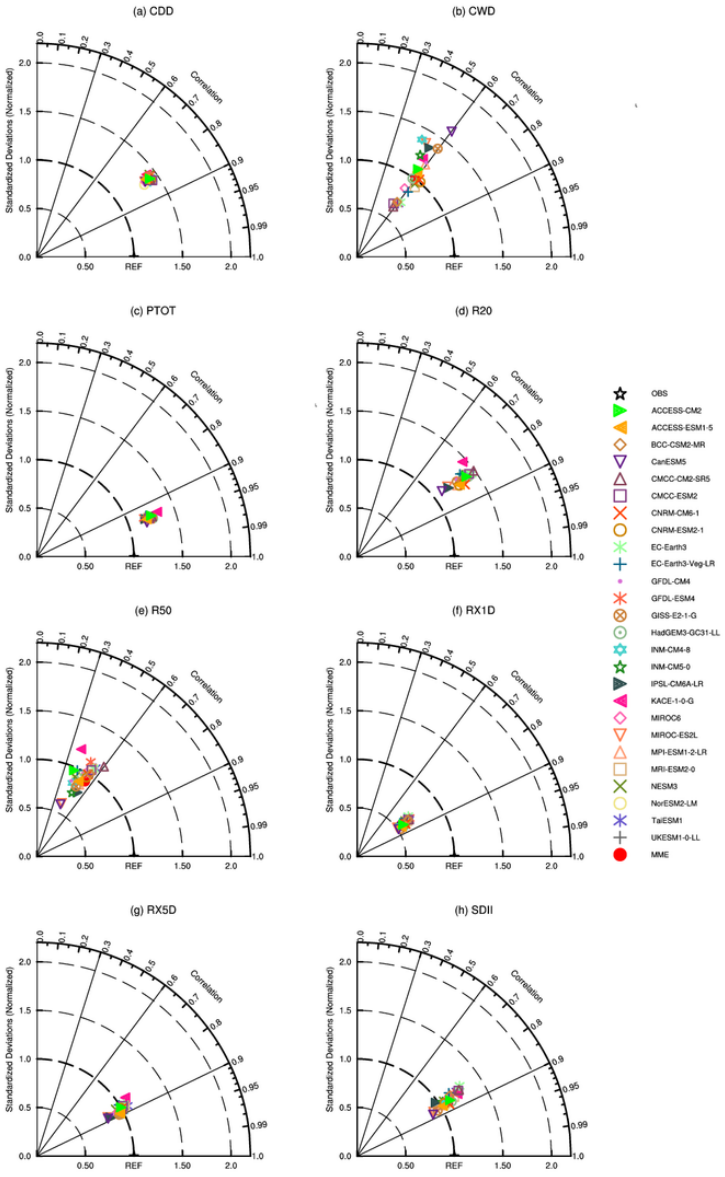

Figure 6

As in Fig. 2 but for eight precipitation indices

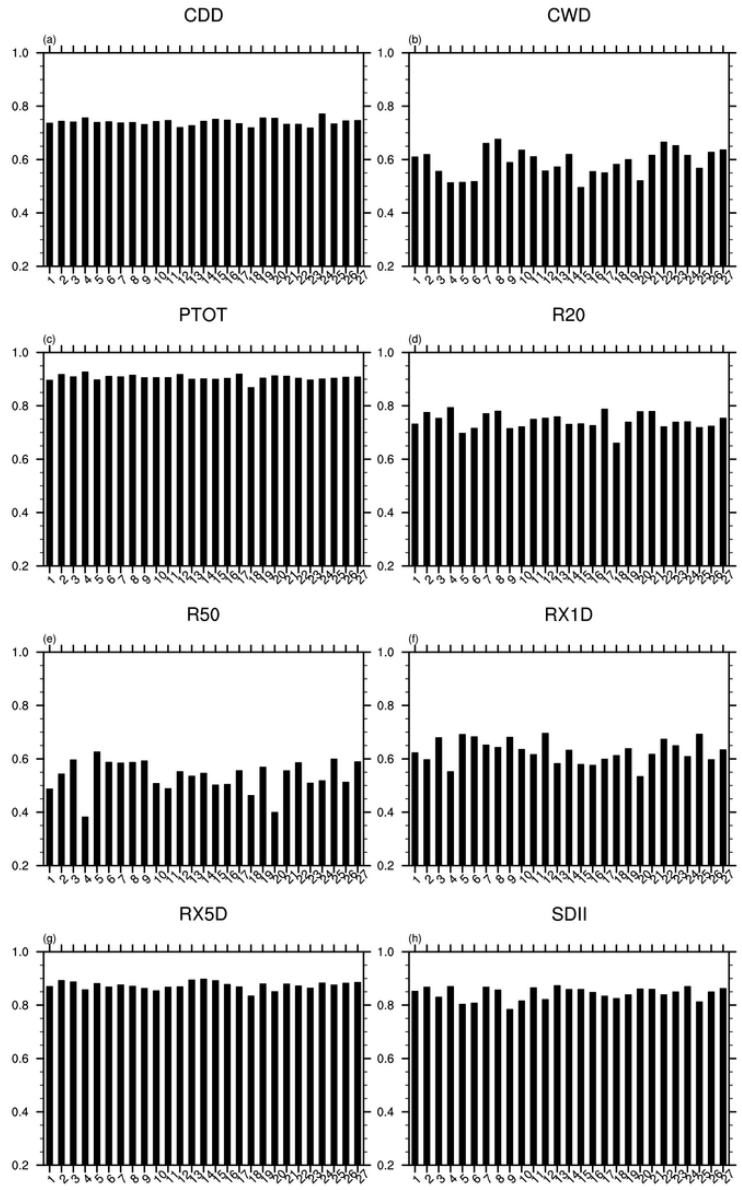

Figure 7

As in Fig. 3 but for eight precipitation indices

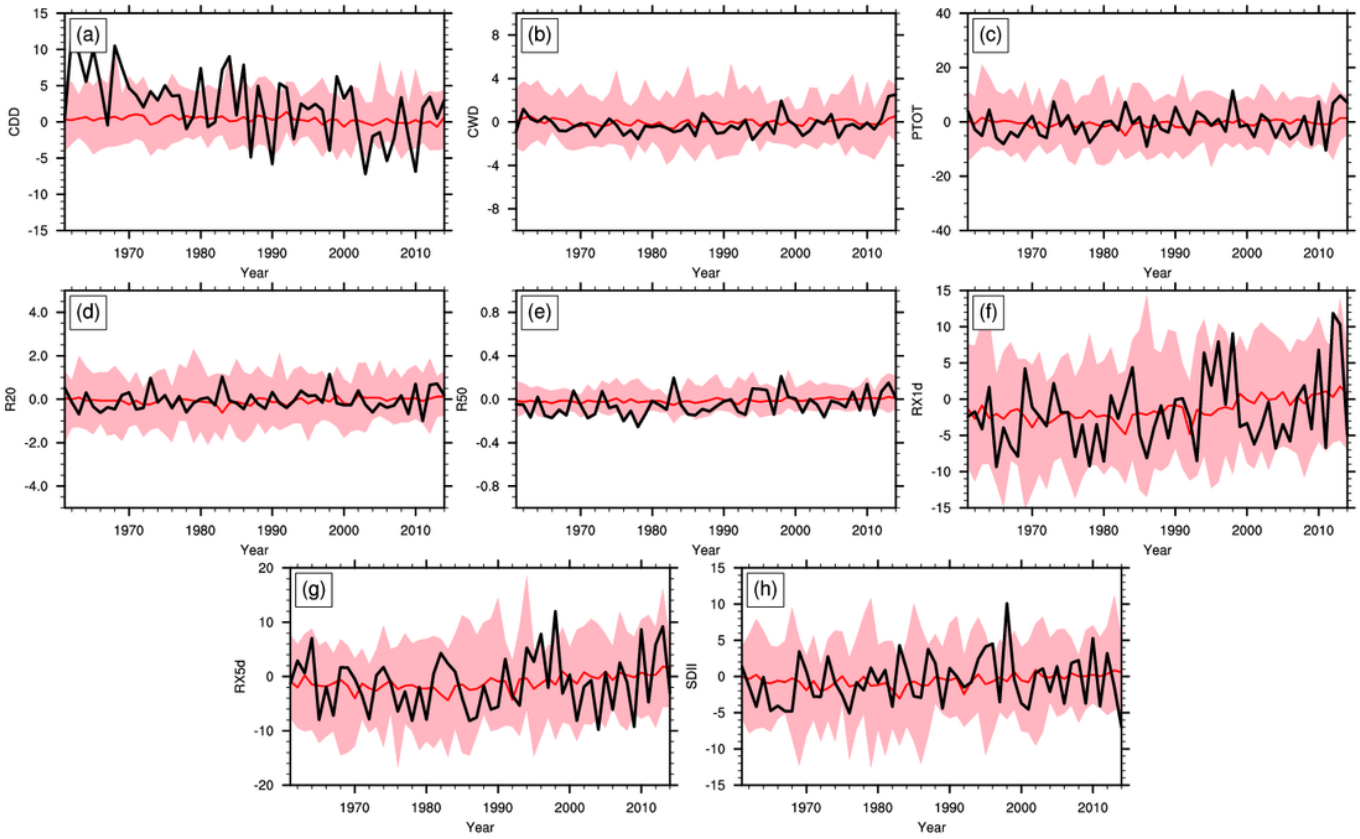

Figure 8

As in Fig. 4 but for eight precipitation indices

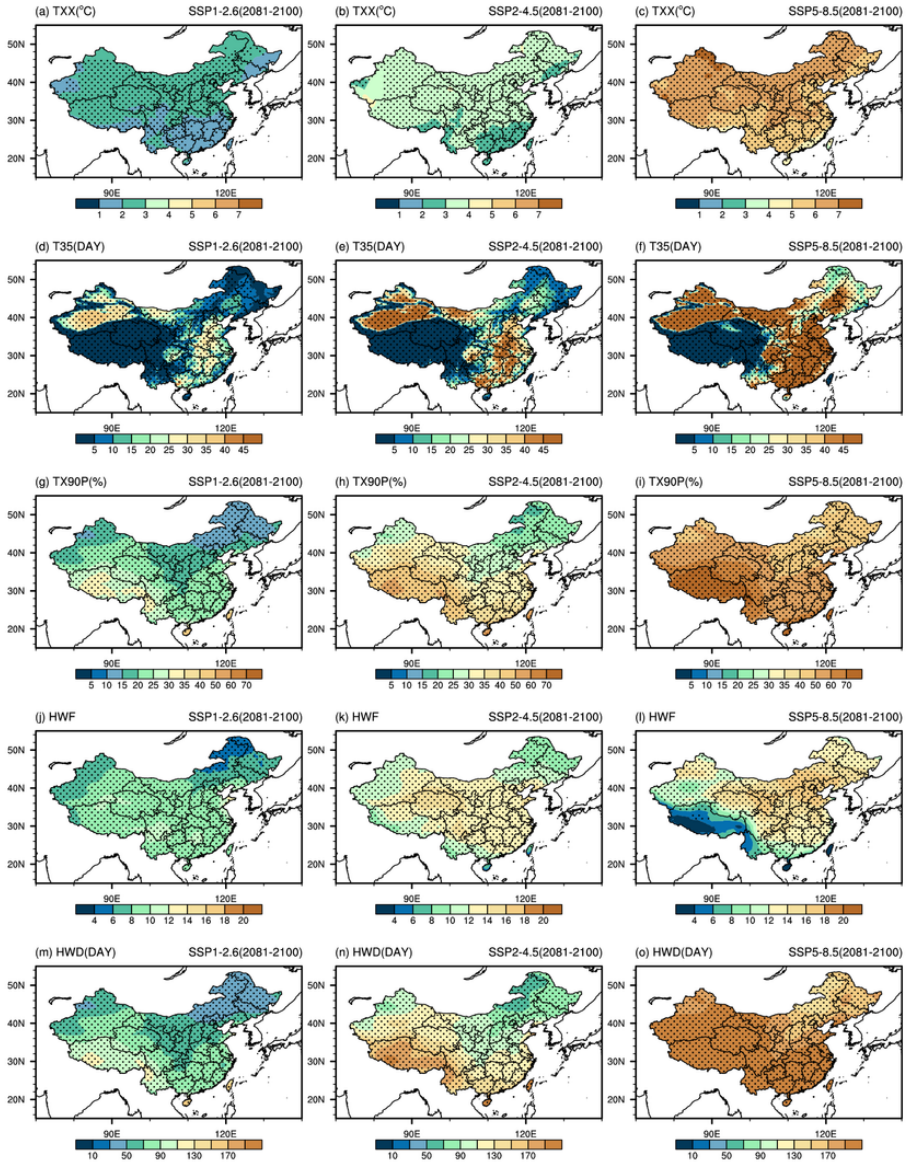

Figure 9

Spatial patterns of the projected changes in TXX, T35, TX90P, HWF and HWD for the NEX-GDDP-CMIP6 MME over China under the SSP1-2.6, SSP2-4.5, and SSP5-8.5 scenarios by the end of the 21st century (2081-2100) relative to the period from 1995 to 2014. The stippling is present in regions where more than 90% of the models are consistent with the signs of MME changes

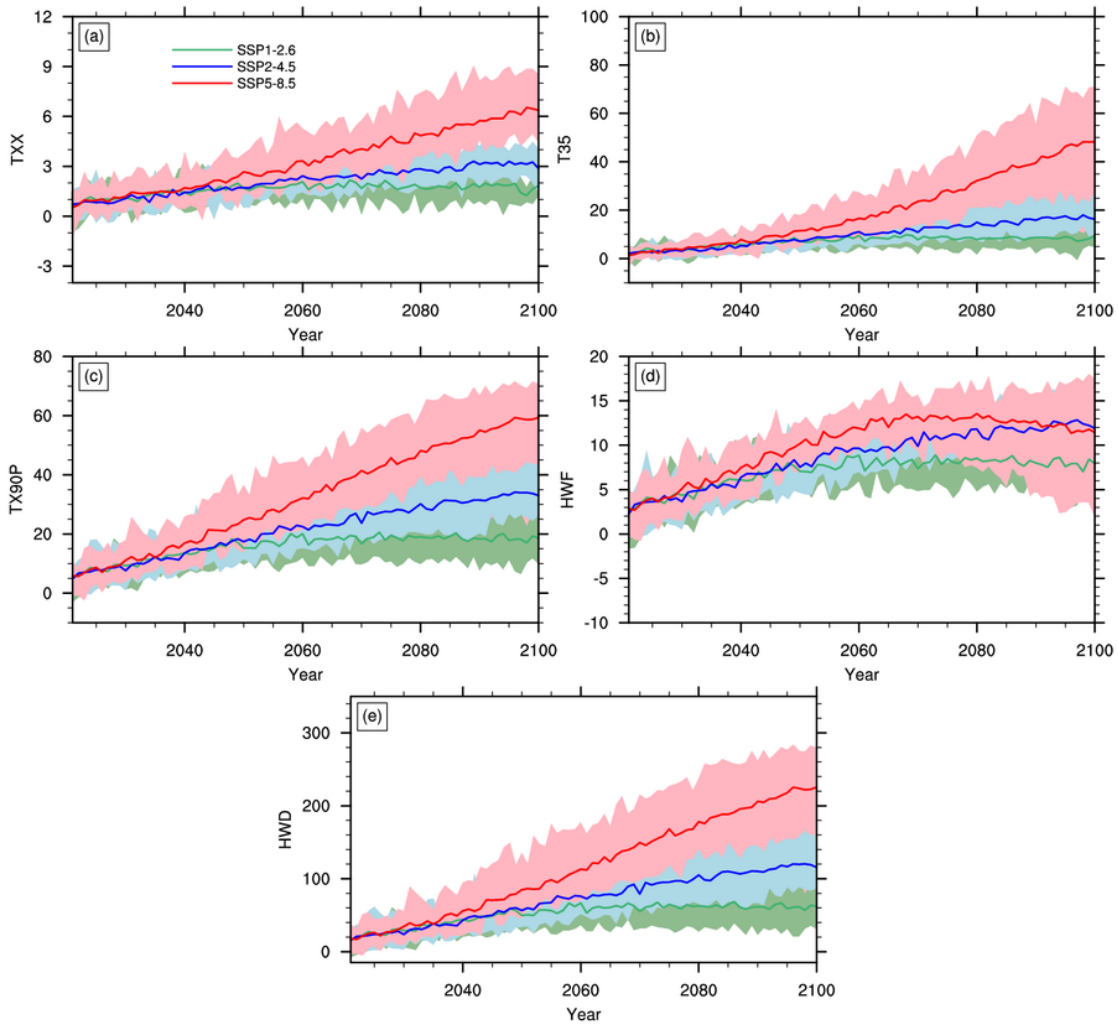

Figure 10

Temporal evolution of the projected changes in (a) TXX, (b) T35, (c) TX90P, (d) HWF, and (e) HWD for the NEX-GDDP-CMIP6 MME over China under the SSP1-2.6, SSP2-4.5 and SSP5-8.5 scenarios for 2015-2100 relative to the reference period 1995-2014. The shading indicates the minimum and maximum values.

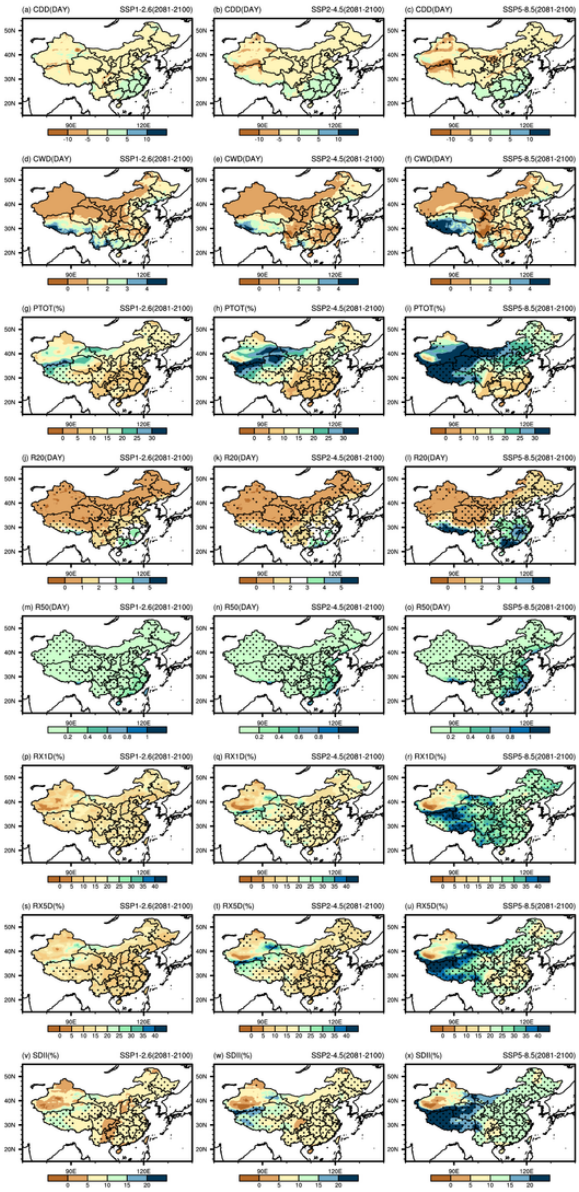

Figure 11

As in Fig. 9 but for eight precipitation indices

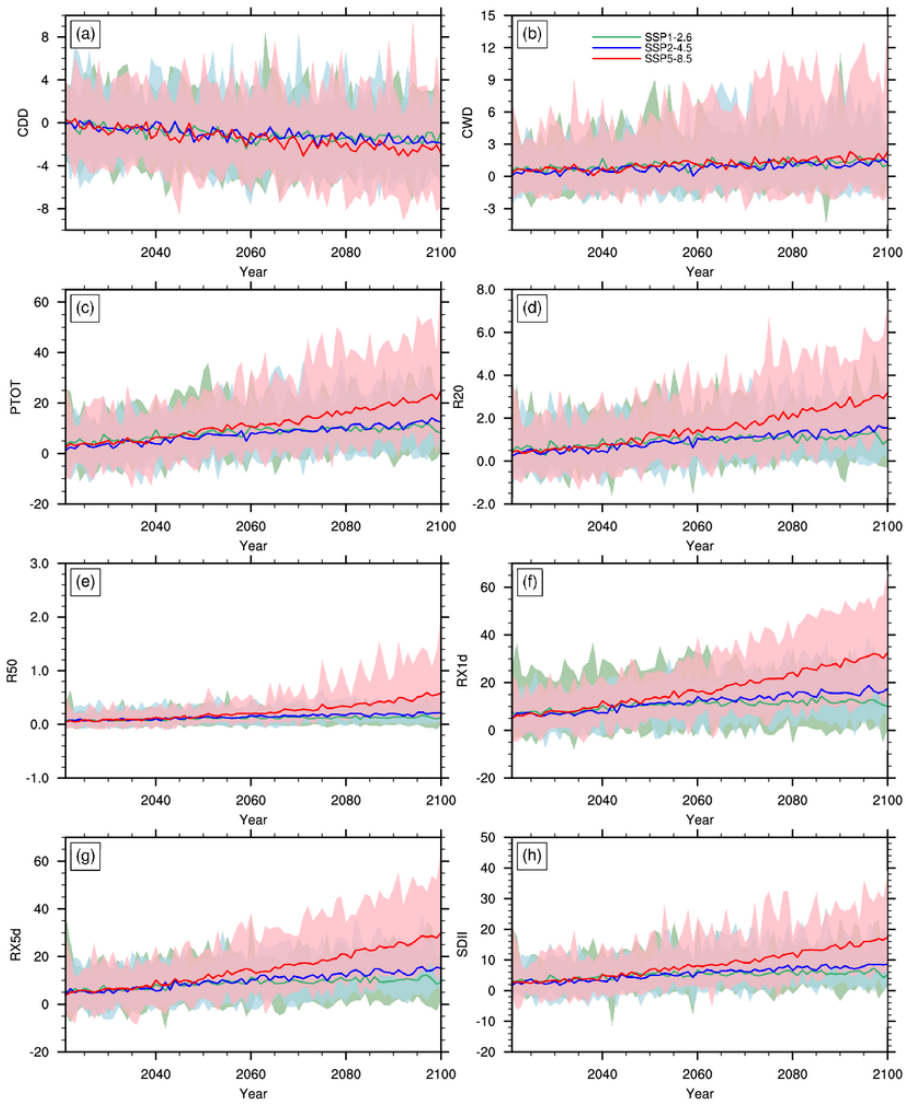

Figure 12

As in Fig. 10 but for eight precipitation indices